

Stellar-mass black holes in the Hyades star cluster?

S. Torniamenti ^{1,2,3}★ M. Gieles ^{4,5} Z. Penoyre ^{6,7} T. Jerabkova,⁸ L. Wang ^{9,10} and F. Anders⁴

¹Physics and Astronomy Department Galileo Galilei, University of Padova, Vicolo dell'Osservatorio 3, I-35122 Padova, Italy

²INFN – Padova, Via Marzolo 8, I-35131 Padova, Italy

³INAF – Osservatorio Astronomico di Padova, Vicolo dell'Osservatorio 5, I-35122 Padova, Italy

⁴Institut de Ciències del Cosmos (ICCUB), Universitat de Barcelona (IEEC-UB), Martí i Franquès 1, E-08028 Barcelona, Spain

⁵ICREA, Pg. Lluís Companys 23, E-08010 Barcelona, Spain

⁶Institute of Astronomy, University of Cambridge, Madingley Road, CB3 0HA Cambridge, UK

⁷Leiden Observatory, Leiden University, PO Box 9513, NL-2300 RA Leiden, the Netherlands

⁸European Southern Observatory, Karl-Schwarzschild-Straße 2, D-85748 Garching bei München, Germany

⁹School of Physics and Astronomy, Sun Yat-sen University, Daxue Road, Zhuhai 519082, China

¹⁰CSST Science Center for the Guangdong-Hong Kong-Macau Greater Bay Area, Zhuhai 519082, China

Accepted 2023 June 20. Received 2023 June 19; in original form 2023 March 17

ABSTRACT

Astrophysical models of binary-black hole mergers in the universe require a significant fraction of stellar-mass black holes (BHs) to receive negligible natal kicks to explain the gravitational wave detections. This implies that BHs should be retained even in open clusters with low escape velocities ($\lesssim 1 \text{ km s}^{-1}$). We search for signatures of the presence of BHs in the nearest open cluster to the Sun – the Hyades – by comparing density profiles of direct N -body models to data from *Gaia*. The observations are best reproduced by models with 2–3 BHs at present. Models that never possessed BHs have an half-mass radius ~ 30 per cent smaller than the observed value, while those where the last BHs were ejected recently ($\lesssim 150 \text{ Myr}$ ago) can still reproduce the density profile. In 50 per cent of the models hosting BHs, we find BHs with stellar companion(s). Their period distribution peaks at $\sim 10^3 \text{ yr}$, making them unlikely to be found through velocity variations. We look for potential BH companions through large *Gaia* astrometric and spectroscopic errors, identifying 56 binary candidates – none of which is consistent with a massive compact companion. Models with 2–3 BHs have an elevated central velocity dispersion, but observations cannot yet discriminate. We conclude that the present-day structure of the Hyades requires a significant fraction of BHs to receive natal kicks smaller than the escape velocity of $\sim 3 \text{ km s}^{-1}$ at the time of BH formation and that the nearest BHs to the Sun are in, or near, Hyades.

Key words: black hole physics – methods: numerical – binaries: general – stars: kinematics and dynamics – star clusters: individual: Hyades cluster.

1 INTRODUCTION

The discovery of binary black holes (BBH) mergers with gravitational wave (GW) detectors (The LIGO Scientific Collaboration 2021) has led to an active discussion on the origin of these systems (for example, Belczynski et al. 2016a; Mandel & de Mink 2016; Rodriguez, Chatterjee & Rasio 2016; Samsing et al. 2022). A popular scenario is that BBHs form dynamically in the centres of globular clusters (GCs, for example, Portegies Zwart & McMillan 2000; Antonini & Gieles 2020a) and open clusters (OCs, for example, Di Carlo et al. 2019; Rastello et al. 2019; Kumamoto, Fujii & Tanikawa 2020; Banerjee 2021; Torniamenti et al. 2022). This scenario has gained support from the discovery of accreting BH candidates in an extragalactic GC (Maccarone et al. 2007) and several Milky Way GCs (Strader et al. 2012; Chomiuk et al. 2013; Miller-Jones et al. 2015) as well as the discovery of three detached binaries with BH

candidates in the Milky Way GC NGC 3201 (Giesers et al. 2018, 2019) and one in the 100 Myr star cluster NGC 1850 in the Large Magellanic Cloud (Saracino et al. 2022, but see El-Badry & Burdge 2022; Saracino et al. 2023).

Various studies have also pointed out that populations of stellar-mass BHs may be present in GCs, based on their large core radii (Mackey et al. 2007, 2008); the absence of mass segregation of stars in some GCs (Alessandrini et al. 2016; Peuten et al. 2016; Weatherford et al. 2020); the central mass-to-light ratio (Baumgardt et al. 2019; Hénault-Brunet et al. 2019; Zocchi, Gieles & Hénault-Brunet 2019; Dickson et al. 2023); the core over half-light radius (Askar, Arca Sedda & Giersz 2018; Kremer et al. 2020), and the presence of tidal tails (Gieles et al. 2021).

Recently, Gieles et al. (2021) presented direct N -body models of the halo GC Palomar 5. This cluster is unusually large ($\sim 20 \text{ pc}$) and is best-known for its extended tidal tails. Both these features can be reproduced by an N -body model that has at present ~ 20 per cent of the total mass in stellar-mass BHs. They show that the half-light radius, R_{eff} , is a strong increasing function of the mass fraction in

* E-mail: stefano.torniamenti@studenti.unipd.it

BHs (f_{BH}). Because all models were evolved on the same orbit, this implies that the ratio of R_{eff} over the Jacobi radius is the physical parameter that is sensitive to f_{BH} .

At the present day, all of the searches for BH populations in star clusters focused on old ($\gtrsim 10$ Gyr) and relatively massive ($\gtrsim 10^4 M_{\odot}$) GCs in the halo of the Milky Way, and there is thus far no work done on searches for BHs in young OCs in the disc of the Milky Way. The reason is that most methods that have been applied to GCs are challenging to apply to OCs: for mass-to-light ratio variations, precise kinematics are required, which is hampered by orbital motions of binaries (Geller, Latham & Mathieu 2015, Rastello, Carraro & Capuzzo-Dolcetta 2020) and potential escapers (Fukushige & Heggie 2000; Claydon, Gieles & Zocchi 2017; Claydon et al. 2019) at the low velocity dispersions of OCs (few 100 m s^{-1}). In the last few years, the advent of the ESA *Gaia* survey (Gaia Collaboration 2016, see Gaia Collaboration 2022 for the latest release) has allowed us, for the first time, to study in detail the position and velocity space of OCs (for example, see Cantat-Gaudin 2022 for a recent review), and to identify their members with confidence. Several hundreds of new objects have been discovered (for example, Cantat-Gaudin et al. 2018a, b; Castro-Ginard et al. 2018, 2020, 2022; Liu & Pang 2019; Sim et al. 2019; Hunt & Reffert 2021; Chi et al. 2023; Hunt & Reffert 2023), and could be distinguished from non-physical overdensities that were erroneously listed as OCs in the previous catalogues (Cantat-Gaudin & Anders 2020).

The possibility to reveal the full spatial extension of OCs members has made it feasible to describe in detail their radial distributions, up to their outermost regions (Tarricq et al. 2022), and to study them as dynamical objects interacting with their Galactic environment. In particular, OCs display extended haloes of stars, much more extended than their cores, which are likely to host a large number of cluster members (Nilakshi et al. 2002; Meingast, Alves & Rottensteiner 2021). Also, evidence of structures that trace their ongoing disruption, like tidal tails, has been found for many nearby OCs, like the Hyades (Reino et al. 2018; Lodieu et al. 2019; Meingast & Alves 2019; Röser, Schilbach & Goldman 2019; Jerabkova et al. 2021), Blanco 1 (Zhang et al. 2020), Praesepe (Röser & Schilbach 2019), and even more distant ones like UBC 274 (Piatti 2020; Casamiquela et al. 2022). This wealth of data provides the required information to characterize the structure of OCs in detail and, possibly, to look for the imprints given by the presence of dark components, in the same way as done for GCs.

In this exploratory study, we aim to find constraints on the presence of BHs in the Hyades cluster, the nearest – and one of the most widely studied – OCs. We use the same approach as in the Palomar 5 study of Gieles et al. (2021), hence a good understanding of the behaviour of R_{eff} at the orbit of the Hyades is required, that is, the model clusters need to be evolved in a realistic Galactic potential. To this end, we explore the large suite of N -body models by Wang & Jerabkova (2021), conceived to model the impact of massive stars (that is, the BH progenitors) on the present-day structure of Hyades-like clusters. By comparing these models to the radial profiles of Hyades members with different masses from *Gaia* (Evans & Oh 2022), we aim to constrain if a BH population is required.

The paper is organized as follows. In Section 2, we describe the details of the N -body models and our method to compare them to observations. In Section 3, we report the results for the presence of BHs in the Hyades. In Section 4, we report a discussion on BH-star candidates in the cluster. Finally, Section 5 summarizes our conclusions.

Table 1. Left: Total mass scale (M_p) and radius scale (a_p) for the two components of the best-fitting Plummer model, from Evans & Oh (2022). Right: the resulting mass (M) and half-mass radius (r_{hm}) for the stars within 10 pc, obtained by truncating the best-fitting Plummer models at $r_t = 10$ pc.

	Plummer parameters		Stars within 10 pc	
	$M_p (M_{\odot})$	$a_p (\text{pc})$	$M (M_{\odot})$	$r_{\text{hm}} (\text{pc})$
Low-mass	117.3	6.21	71.9	5.67
High-mass	207.5	3.74	170.5	4.16

2 METHODS

2.1 The Hyades cluster

The Hyades is the nearest OC to us, at a distance $d \approx 45$ pc (Perryman et al. 1998). By relying on 6D phase-space constraints, Röser et al. (2011) identified 724 stellar members moving with the bulk Hyades space velocity, with a total mass of $435 M_{\odot}$ (Röser et al. 2011). The tidal radius is estimated to be $r_t \approx 10$ pc, and the resulting bound mass is $\approx 275 M_{\odot}$ (Röser et al. 2011). Also, the cluster displays prominent tidal tails, which extend over a distance of 800 pc (Jerabkova et al. 2021).

The Hyades contains stars with masses approximately between $0.1 M_{\odot}$ and $2.6 M_{\odot}$. Röser et al. (2011) found that average star mass of the cluster decreases from the centre to the outward regions, as a consequence of mass segregation. Recently, Evans & Oh (2022) performed a detailed study of the Hyades membership and kinematics, with the aim to quantify the degree of mass segregation within the cluster. In particular, they applied a two-component mixture model to the *Gaia* DR2 data (Gaia Collaboration 2018a) and identified the cluster and tail members with masses $m > 0.12 M_{\odot}$ (brighter than $m_G < 14.06$). They assigned a mass value to each observed source through a nearest neighbour interpolation on the *Gaia* colour-magnitude space (BP–RP versus m_G). Finally, they defined two components, named ‘high-mass’ and ‘low-mass’ stars, based on a colour threshold at BP–RP = 2, corresponding to $0.56 M_{\odot}$. The component median masses are $0.95 M_{\odot}$ and $0.32 M_{\odot}$, respectively. These values were taken as nominal masses for the two components.

Because of mass segregation, this two-component formalism has turned out to be required to adequately describe the radial cumulative mass profiles over the entire radius range and within the tidal radius (Evans & Oh 2022). In particular, the mass distributions of the stellar components within 10 pc are well described by a superposition of two Plummer (1911) models. Table 1 reports the parameters of the best-fitting Plummer model (Evans & Oh 2022). The estimated total mass and half-mass radius of stars inside the tidal radius are $M_1 = 71.9 M_{\odot}$ and $r_{\text{hm},1} = 5.7$ pc for the low-mass component, and $M_h = 170.5 M_{\odot}$ and $r_{\text{hm},h} = 4.16$ pc for the high-mass stars.

In this work, we will use the density profiles given by the best-fitting Plummer models reported in Table 1 as observational points to compare to our N -body models. For this reason, hereafter we will refer to these best-fitting profiles as to ‘observed profiles’.

2.2 N -body models

We use the suite of N -body simulations introduced in Wang & Jerabkova (2021), which aim to describe the present-day state of the Hyades cluster. The simulations are generated by using the N -body code PETAR (Wang, Nitadori & Makino 2020a; Wang et al. 2020b), which can provide accurate dynamical evolution of close encounters and binaries. The single and binary stellar evolution

are included through the population synthesis codes SSE and BSE (Hurley, Pols & Tout 2000; Hurley, Tout & Pols 2002; Banerjee et al. 2020).

The ‘rapid’ supernova model for the remnant formation and material fallback from Fryer et al. (2012), along with the pulsational pair-instability supernova from Belczynski et al. (2016b), are used. In this prescription, if no material falls back onto the compact remnant after the launch of the supernova explosion, natal kicks are drawn from the distribution inferred from observed velocities of radio pulsars, that is a single Maxwellian with $\sigma = 265 \text{ km s}^{-1}$ (Hobbs et al. 2005). For compact objects formed with fallback, kicks are lowered proportionally to the fraction of the mass of the stellar envelope that falls back (f_b). In this case $v_{\text{kick, fb}} = (1 - f_b)v_{\text{kick}}$, where v_{kick} is the kick velocity without fallback. For the most massive BHs that form via direct collapse ($f_b = 1$) of a massive star, no natal kicks are imparted. In this formalism, the kick is a function of the fallback fraction, and not of the mass of the compact remnant. In this recipe and for the adopted metallicity of $Z = 0.02$, about 45 per cent (50 per cent) of the formed BH number (mass) has $f_b = 1$, and therefore does not receive a natal kick.

The tidal force from the Galactic potential is calculated through the GALPY code (Bovy 2015) with the MWPotential2014. This prescription includes a power-law density profile with an exponential cut-off for the bulge, a Miyamoto & Nagai (1975) disc, and a NFW profile (Navarro, Frenk & White 1995) for the halo.

2.2.1 Initial conditions

The suite of N -body models consists of 4500 star clusters, initialized with a grid of different total masses M_0 and half-mass radii $r_{\text{hm},0}$. The initial values for M_0 are set to 800, 1000, 1200, 1400, or 1600 M_\odot , while $r_{\text{hm},0}$ takes values 0.5, 1, or 2 pc. The initial positions and velocities are sampled from a Plummer (1911) sphere, truncated at the tidal radius (see below).

The cluster initial mass function (IMF) is sampled from a Kroupa (2001) IMF between 0.08 and 150 M_\odot . For each couple $[M_0, r_{\text{h},0}]$, Wang & Jerabkova (2021) generate 300 models by randomly sampling the stellar masses with different random seeds. On the one hand, this allows us to quantify the impact of stochastic fluctuations in the IMF sampling, which, for clusters with a limited number of particles, are generally large (for example, see Goodman, Hogg & Hut 1993; Boekholt & Portegies Zwart 2015; Wang & Hernandez 2021). On the other hand, different random samplings result in different fractions of O-type stars with $m > 20 M_\odot$ (the BH progenitors), which deeply affect the cluster global evolution (see Wang & Jerabkova 2021).

In the models considered, the mass fraction of O-type stars f_O ranges from 0 to 0.34 (the expected fraction for the chosen IMF is 0.13). The stochasticity of the mass sampling may result in clusters with $f_O = 0$, meaning that they do not contain stars massive enough to form BHs at all. The percentage of clusters with $f_O = 0$ depends on the initial cluster mass, and varies from 6 per cent for clusters with $M_0 = 800 M_\odot$ to 0.7 per cent for clusters with $M_0 = 1600 M_\odot$. Overall, 2.4 per cent of the clusters do not host stars with $m > 20 M_\odot$. No primordial binaries are included in the simulations (see the discussion in Section 4.2).

All the clusters are evolved for 648 Myr, the estimated age of the Hyades (Wang & Jerabkova 2021). The initial position and velocity of the cluster are set to match the present-day coordinates in the Galaxy (see Gaia Collaboration 2018b; Jerabkova et al. 2021). For this purpose, the centre of the cluster is first integrated backwards for 648 Myr in the MWPotential2014 potential by means of the

time-symmetric integrator in GALPY. The final coordinates are then set as initial values for the cluster position and velocity (Wang & Jerabkova 2021). The resulting initial tidal radius is (see also fig. 5 in Wang, Tanikawa & Fujii 2022):

$$r_{\text{t},0} \approx 12 \left[\frac{M_0}{1000 M_\odot} \right]^{1/3} \text{ pc}, \quad (1)$$

while the tidal filling factor, defined as $r_{\text{hm},0} / r_{\text{t},0}$, spans from 0.03 to 0.18. Stars that initially lie outside the tidal radius are removed from the cluster.

2.3 Comparing models to observations

We build the model density profiles from the final snapshots of the N -body simulations. First, we centre the cluster to the density centre, calculated as the square of density weighted average of the positions (Casertano & Hut 1985; Aarseth 2003). Then, we build the profiles for low-mass and high-mass stars within r_t , separately. To be consistent with the observed profiles (see Section 2.1), we define all the stars below 0.56 M_\odot as low-mass stars, and all the luminous main-sequence and post-main sequence stars above this threshold as high-mass stars. Also, because we want to compare to observable radial distributions, we only include the visible components of the cluster (main sequence and giant stars), without considering white dwarfs, neutron stars, and BHs. We divide the stellar cluster into radial shells containing the same number of stars. Due to the relatively low number of stars, we consider $N_{\text{bin}} = 10$ stars per shell.

To assess how well the models reproduce the observed profiles, we refer to a χ^2 comparison, where we define the reduced χ^2 , χ_v^2 (with an expected value near 1), as:

$$\chi_v^2 = \frac{1}{\nu} \sum_i \frac{(\rho_{\text{obs},i} - \rho_{\text{mod},i})^2}{\delta \rho_i^2}, \quad (2)$$

where ν is the number of degrees of freedom, which depends on the number of density points obtained with the binning procedure. The quantities $\rho_{\text{obs},i}$ and $\rho_{\text{mod},i}$ are the density in the i^{th} bin for the observed and model profile, respectively. The error $\delta \rho_i^2$ is given by the sum of the model and the observed bin uncertainties. For both observed and N -body profiles, we determine the uncertainty as the Poisson error:

$$\delta \rho = \frac{\bar{m}}{4/3 \pi (r_f^3 - r_i^3)} \sqrt{N_{\text{bin}}}, \quad (3)$$

where \bar{m} is the mean mass of the bin stars, and r_i^3 and r_f^3 are the bin upper and lower limit. For the N -body models, the bin lower (upper) limit is set as the position of the innermost (outermost) star, and \bar{m} is the mean stellar mass in each bin. For the observed profiles, we consider the same bin boundaries as the N -body models, and set \bar{m} to the nominal mass of the component under consideration. Then, we estimate analytically from the Plummer (1911) distribution the number of stars between r_i and r_f and the corresponding uncertainty.

Our comparison is performed by considering the high-mass density profile only. This choice is motivated by the fact that the observed mass function in fig. 2 of Evans & Oh (2022) displays a depletion below 0.2 M_\odot , which may hint at possible sample incompleteness. We thus focus only on the high-mass range to obtain a more reliable result. Also, high-mass stars, being more segregated, represent better tracers of the innermost regions of the cluster, where BHs are expected to reside, and thus provide more information about the possible presence of a dark component. We emphasize that this

is intended as a formal analysis with the objective of determining whether a model is able to give a reasonable description of the observed cluster profile.

In order to filter out the simulations that present little agreement with the observations, we consider only the models with a final high-mass bound mass within $\pm 20 M_{\odot}$ from the observed value of $M_h = 170.5 M_{\odot}$ (see Table 1). Among the simulated models, 636 clusters (14 per cent of all the N -body models) lie within this mass range.

3 RESULTS

As the cluster tends towards a state of energy equipartition, the most massive objects progressively segregate toward its innermost regions, while dynamical encounters push low-mass stars further and further away (Spitzer 1987). BHs, being more massive than any of the stars, tend to concentrate at the cluster centre, quenching the segregation of massive stars. As a consequence, their presence in a given star cluster is expected to affect the radial mass distribution of the cluster's stellar population (Fleck et al. 2006; Hurley 2007; Alessandrini et al. 2016; Peuten et al. 2016; Weatherford et al. 2020). In the star cluster sample under consideration, the number of BHs within 10 pc, N_{BH} , ranges from 0 to 5. Star clusters with $N_{\text{BH}} = 0$ can result from the ejection of all the BHs, because of supernovae kicks (50 per cent of the cases) and/or as the result of dynamical interactions. As for supernovae kicks, since our N -body models have initial escape velocities $v_{\text{esc}} \lesssim 6 \text{ km s}^{-1}$, which decrease to $v_{\text{esc}} \lesssim 3 \text{ km s}^{-1}$ at 24 Myr, only BHs formed with kicks lower than 3 km s^{-1} can be retained (see also Pavlík et al. 2018). Also, as mentioned earlier, the IMF may not contain stars massive enough to form BHs (12 per cent of the models within the mass cut that end up with 0 BHs, see Section 2.2).

In the following, we will assess if $N_{\text{BH}} \leq 5$ BHs can produce quantifiable imprints on the radial distributions of stars.

3.1 χ^2_v distributions

Fig. 1 shows the distributions of χ^2_v for different N_{BH} . If we apply the mass cut introduced in Section 2.3, we automatically select most of the models with χ^2_v closer to the expected value near 1, and remove those that are highly inconsistent with the observed profiles. The result of our comparison improves with increasing the number of BHs up to $N_{\text{BH}} = 4$, which however applies to only 1 per cent of the cases. If we focus on the cases with a large number of good fits ($N_{\text{BH}} \leq 3$), the median value of the reduced chi-squared distributions decrease from $\chi^2_v \approx 3$ to $\chi^2_v \approx 1$ for N_{BH} increasing from 0 to 3.

When only models within the mass cut are considered, they have $N_{\text{BH}} \leq 3$ in 98 per cent of the cases. This is mainly because star clusters that contain a high initial mass fraction in O-type stars (which evolve into BHs) are easily dissolved by the strong stellar winds (Wang & Jerabkova 2021), and result in present-day cluster masses far below the observed one. If the initial mass fraction in O-type stars is more than twice as high as that expected from a Kroupa (2001) IMF, our models cannot produce clusters in the selected mass range.

Table 2 reports the final relevant masses and mass fractions of the N -body models, for different values of N_{BH} . In all the cases, the total mass in high-mass stars is $\approx 170 M_{\odot}$, as a consequence of the chosen criterion for filtering out models with little agreement with the observed cluster. The total visible mass, $M_{\text{vis}} \approx 240 M_{\odot}$, does not show any dependence on N_{BH} , with the only exception of the sample

with 5 BHs. For the latter case, as mentioned earlier, the initial larger mass fraction of O-stars brings about a more efficient mass-loss across the tidal boundary, and results in lower cluster masses. In contrast, the total mass M_{tot} increases with N_{BH} : the mass in BHs spans from $\approx 10 M_{\odot}$ ($f_{\text{BH}} = 0.04$) when $N_{\text{BH}} = 1$, to $\approx 45 M_{\odot}$ for the case with 5 BHs ($f_{\text{BH}} = 0.16$).

3.2 Two-component radial distributions

To highlight the difference between models with and without BHs, we randomly draw 16 models from simulations (within the mass cut) with 0 BHs and from a sample obtained by combining the sets with 2 and 3 BHs. For each distribution, we evaluated the median values for selected bins and the spread, as $1.4 \times \text{MAD} (\sqrt{N_{\text{bin}}})^{-1}$, where MAD is the median absolute deviation.

Fig. 2 displays the density profiles of the high-mass (top) and low-mass (bottom) stars of these samples, compared to the observed profiles (see Section 2.1). The density profiles of the N -body models with BHs are mostly consistent with the observed distributions. High-mass stars in clusters with $N_{\text{BH}} = 0$ display a more concentrated distribution reminiscent of the cusped surface brightness profiles of core collapsed GCs (Djorgovski & King 1986). The models with BHs have cored profiles, which Merritt et al. (2004) attributed to the action of a BH population. Although in our models there are only 2 or 3 BHs, it has been noticed already by Hurley (2007) that a single BBH is enough to prevent the stellar core from collapsing. It is worth noting that the Plummer models that were fit to the observations are cored and would therefore not be able to reproduce a cusp in the observed profile. But from inspecting the cumulative mass profile in fig. 3 of Evans & Oh (2022) we see that the observed profile follows the cored Plummer model very well, with hints of a slightly faster increase in the inner 1 pc of the high-mass components, compatible with what we see in the top right-hand panel of Fig. 2.

The density profile of low-mass stars is also well described by models with BHs, although they were not included in the fitting procedure. This component presents central densities lower than high-mass stars of about an order of magnitude, as a consequence of mass segregation within the cluster. A better description of the relative concentration of stars with different masses (and thus of the degree of mass segregation) is given by the ratio of their half-mass radii (for example, see Vesperini et al. 2013; de Vita, Bertin & Zocchi 2016; Vesperini et al. 2018; Torniamenti, Bertin & Bianchini 2019). Fig. 3 displays the ratio of the half-mass radius¹ of high-mass to that of low-mass stars, for all the models with 0 BHs and with 2–3 BHs. For the latter case, BHs produce less centrally concentrated distributions of visible stars, and trigger a lower degree of mass segregation. Also, models with BHs yield a much better agreement with the observed value.

3.3 Half-mass radii

Fig. 4 shows the impact of BHs on r_{hm} , defined as the half-mass radius of all the visible stars. The distributions shift towards higher values for increasing numbers of BHs, which is because r_{hm} is larger, but also because of the quenching of mass segregation of the visible components. Our models suggest that 3 BHs can produce

¹In this study, the half-mass radii are calculated from the distributions of the stars within r_c , and do not refer to the half-mass radii of the whole Plummer model.

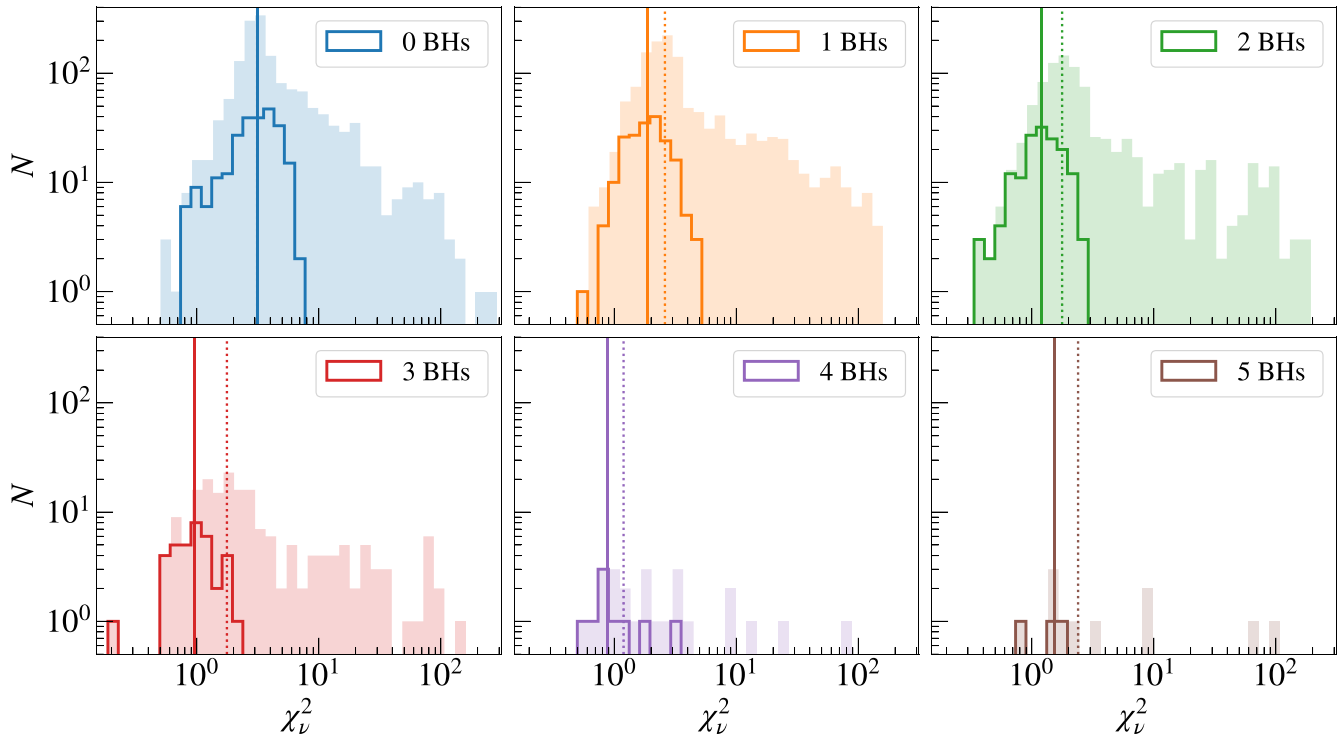


Figure 1. Distributions of χ_v^2 from the fits to the density profiles for star clusters with different numbers of BHs in the Hyades at the present day. The filled area include the entire distributions of star clusters, while the solid line displays the star clusters with $150 M_\odot \leq M_h \leq 190 M_\odot$. The vertical lines show the median value of the distributions when all the clusters are considered (dotted line) and when the mass cut is applied (solid line). In the models with 0 BHs, the two lines overlap.

a ~ 40 per cent increase in the expected value of r_{hm} . As a further hint on the presence of a BH component, the observed value almost coincides with the expected value for $N_{\text{BH}} = 3$.

The r_{hm} distribution of the $N_{\text{BH}} = 0$ sample is mostly inconsistent with the observed value of the Hyades cluster. Unlike the other cases, this distribution shows a more asymmetric shape, with a peak at $r_{\text{hm}} \simeq 3$ pc, and a tail which extends towards larger values. We investigated if this tail may come from clusters that have recently ejected all their BHs, and have still memory of them. Fig. 5 shows the the distribution of the half-mass radii for the cases without BHs at the present day. We distinguished between different ranges of t_{BH} , defined as the time at which the last BH was present within the cluster. The stellar clusters that have never hosted BHs, because they are ejected by the supernova kick or because there are no massive stars to produce them (see Section 3), constitute the bulk of the distribution. These models end up to be too small with respect to the Hyades, and thus are not consistent with the observations, regardless of their M_0 and $r_{\text{hm},0}$ (see also the discussion in Section 4.1). From Fig. 5 we also see that the N -body models where all the BHs were ejected in the first 500 Myr show the same r_{hm} distribution as those that have never hosted BHs. For these clusters, the successive dynamical evolution has erased the previous imprints of BHs on the observable structure, because the most massive stars had enough time to segregate to the centre after the ejection of the last BH.

Finally, star clusters where BHs were present in the last ~ 150 Myr, but are absent at present, preserved some memory of the ejected BH population, and display larger r_{hm} , in some cases consistent with the observed value. Since the present-day relaxation time (Spitzer 1987) for our N -body models is $t_{\text{rlx}} \approx 45$ Myr, we find that the only

models that have ejected their last BH less than $3 t_{\text{rlx}}$ ago can have radii similar to models with BHs.

BHs that were ejected from the Hyades in the last 150 Myr display a median distance ~ 60 pc from the cluster (~ 80 pc from the Sun). Only in two cases, the dynamical recoil ejected the BH to a present-day distance > 1 kpc, while in all the other cases the BH is found closer than 200 pc from the cluster centre.

3.4 High-mass stars parameter space

As explained in Section 3.3, the presence of even 2–3 BHs has a measurable impact on the observable structure of such small-mass clusters. High-mass stars are most affected by the presence of BHs, because they are prevented from completely segregating to the cluster core. In Fig. 6 we show how the number of BHs within the cluster relates to the total mass in high-mass stars (M_h) and to their half-mass radius ($r_{\text{hm},h}$). In this case, we consider all the simulated models, without any restriction on the high-mass total mass, and we show how the average number of BHs in the N -body models varies in the $M_h - r_{\text{hm},h}$ space.

The total mass in high-mass stars can be as high as $400 M_\odot$, while the half-mass radius takes values from 1 to 8 pc. The most diluted clusters feature the lowest mass, because they are closer to being disrupted by the Galactic tidal field. In contrast, models with higher M_h are characterized by the fewest BHs, because of the absence of massive progenitors, which enhance the cluster mass-loss. As explained in Section 3.2, $r_{\text{hm},h}$ grows for increasing number of BHs at the cluster centre. In the Hyades mass range, the expected value of $r_{\text{hm},h}$ when $N_{\text{BH}} = 3$ is larger by almost ~ 60 per cent with

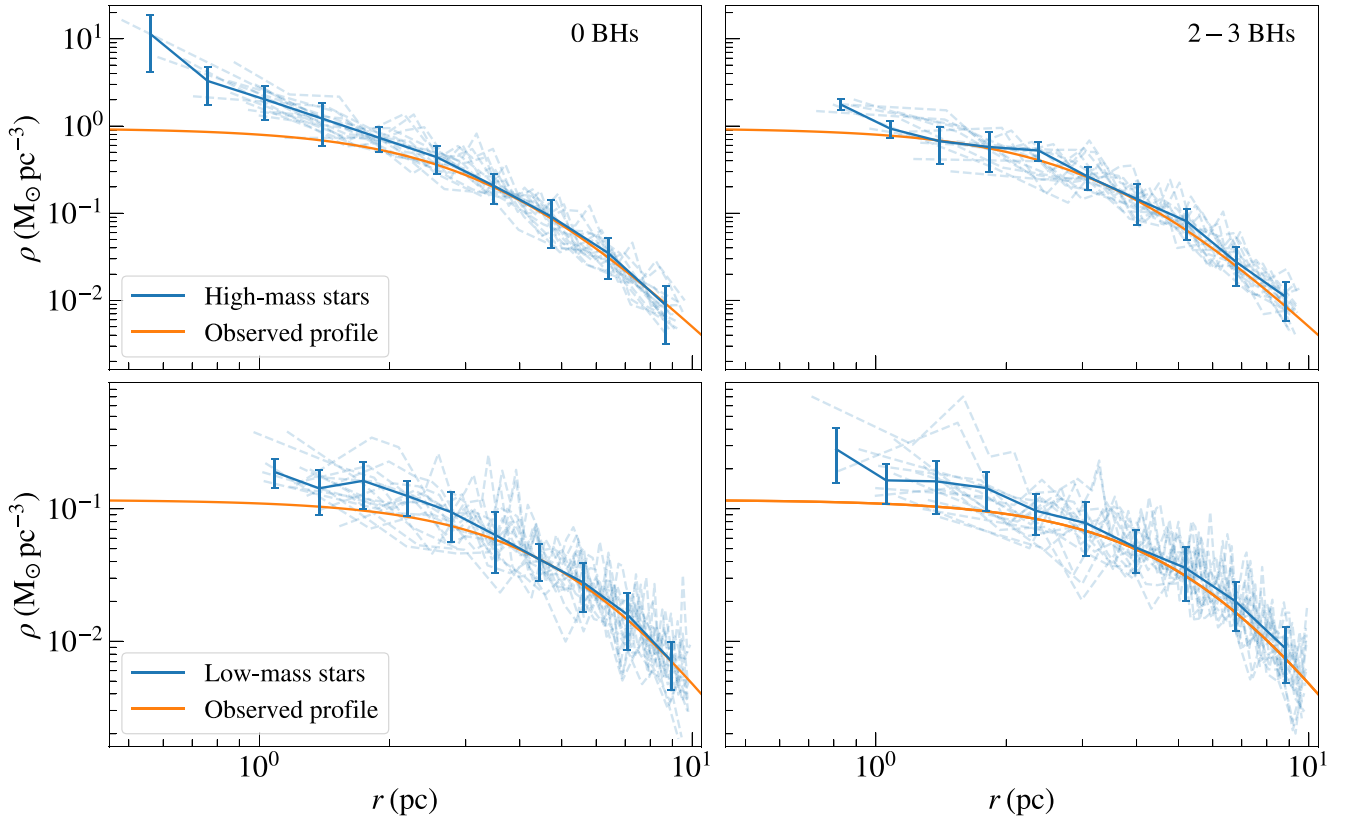


Figure 2. Density profiles for high-mass stars (upper panels) and low-mass stars (lower panels), for 16 models drawn from the cases with $N_{\text{BH}} = 0$ (left-hand panel) and $N_{\text{BH}} = 2-3$ (right-hand panel). The blue dashed lines are the individual models. The blue solid line is the median of the distribution at selected radial distances, with the associated errors. The Plummer uncertainties are comparable to those of the N -body models. The orange line is the observed profile (Evans & Oh 2022).

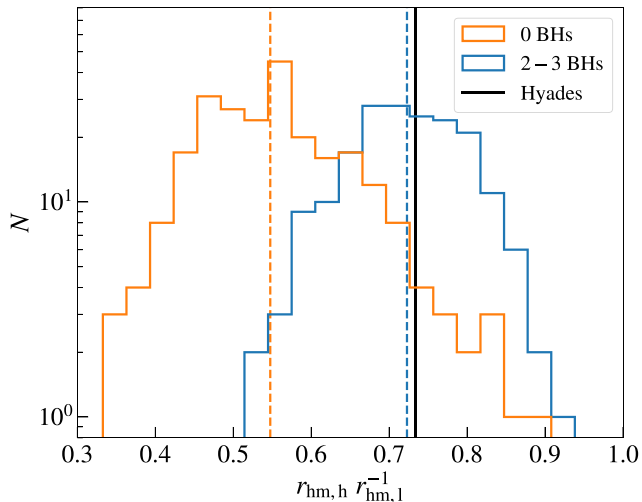


Figure 3. Ratio of the half-mass radius of the high-mass stars ($r_{\text{hm,h}}$) to that of low-mass stars ($r_{\text{hm,l}}$), for star clusters with $N_{\text{BH}} = 0$ (orange) and $N_{\text{BH}} = 2-3$ (blue). The dashed vertical lines represent the medians of the distributions, and the vertical black line displays the observed value for the Hyades (Evans & Oh 2022).

respect to the case with 0 BHs. The observed values (Evans & Oh 2022) lie in a region of the parameter space between 2 and 3 BHs, a further corroboration of the previous results of Section 3. Finally, higher numbers of BHs are disfavoured by our models, because they

predict an even lower degree of mass segregation for high-mass stars.

3.5 Velocity dispersion profiles

We quantified the impact of central BHs on the velocity dispersion profile. To this purpose, we compared the profiles obtained from the samples of 16 models with $N_{\text{BH}} = 0$ and with $N_{\text{BH}} = 2-3$ introduced in Section 3.2. Fig. 7 displays the resulting velocity dispersion profiles, calculated as the mean of the dispersions of the three velocity components. The presence of 2–3 BHs produces a non-negligible increase of 40 per cent in the inner 1 pc.

The rise in dispersion is reminiscent of the velocity cusp that forms around a single massive object (Bahcall & Wolf 1976). Such a cusp develops within the sphere of influence of a central mass, which can be defined as GM_{\bullet}/σ^2 , with M_{\bullet} the mass of the central object and σ the stellar dispersion. For $M_{\bullet} = 20 M_{\odot}$ and $\sigma = 0.3 \text{ km s}^{-1}$ we find that this radius is ~ 1 pc, roughly matching the radius within which the dispersion is elevated. Although a BBH of $20 M_{\odot}$ constitutes ~ 10 per cent of the total cluster mass, the mass with respect to the individual stellar masses is much smaller (factor of 20) compared to the case of an intermediate-mass BH in a GC (factor of 10^4) or a supermassive BH in a nuclear cluster (factor of 10^6). As a result, a BBH in Hyades makes larger excursions from the centre due to Brownian motions. From equation (90) in Merritt (2001) we see that the wandering radius of a BBH of $20 M_{\odot}$ in Hyades is ~ 0.15 pc. Although this is smaller than the sphere of influence, it is still a

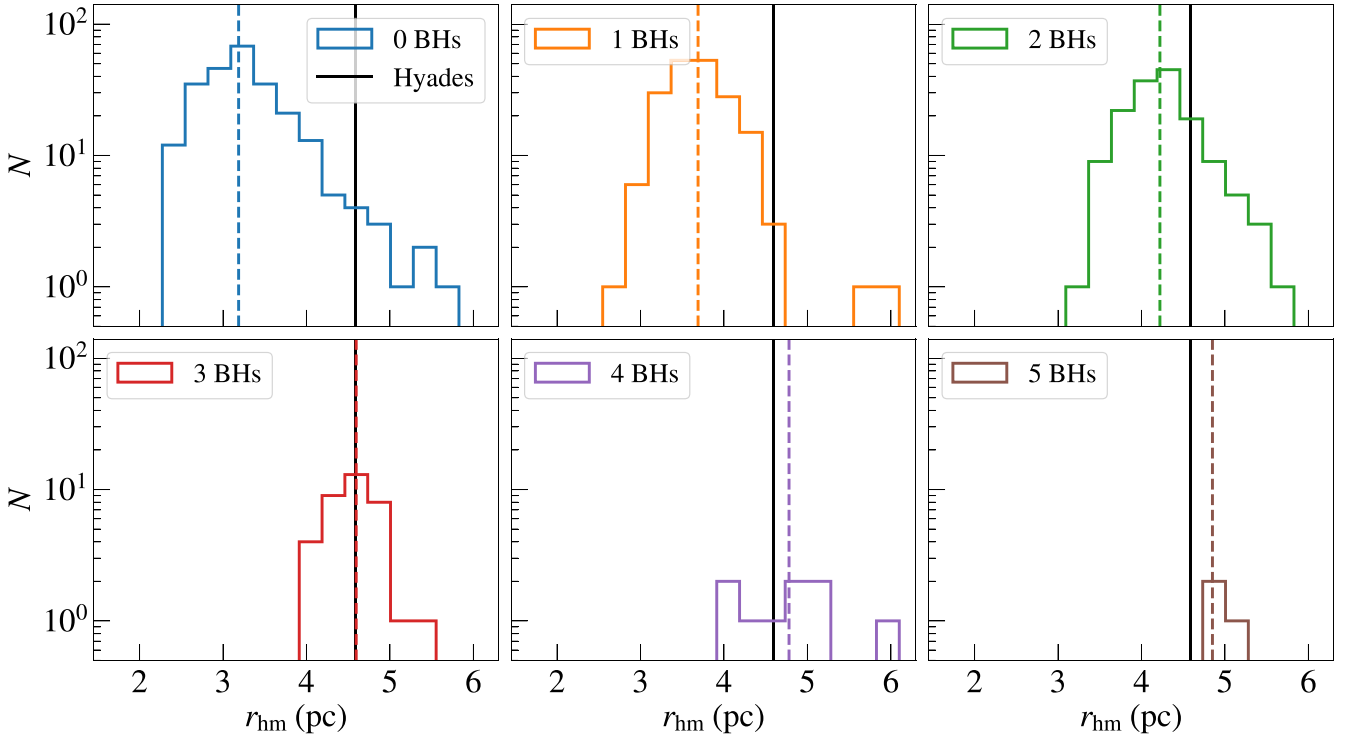


Figure 4. Distributions of half-mass radii of visible stars for N -body models with different N_{BH} . The dashed vertical lines represent the medians of the distributions, and the vertical black line displays the observed value for the Hyades (Evans & Oh 2022).

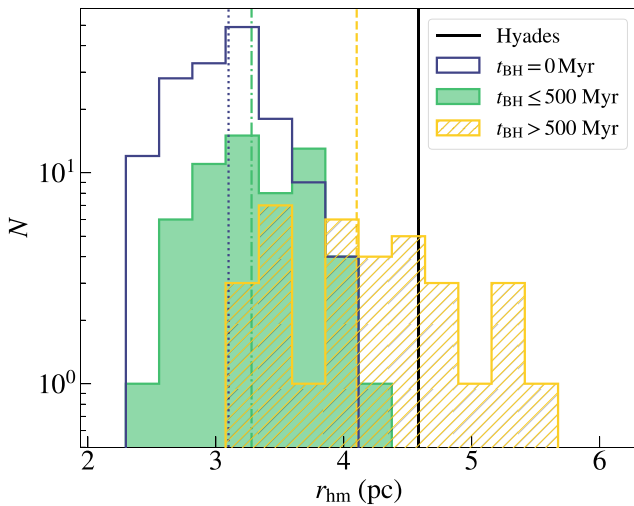


Figure 5. Distributions of r_{hm} for star clusters with no BHs. We distinguish between N -body models where BHs have never been present, because they were ejected by their natal kicks or there were not stars massive enough (purple, vertical dotted line), star clusters where BHs were ejected before 500 Myr (green filled area, vertical dash-dotted line), and star clusters where BHs were ejected after 500 Myr (yellow hatched area, vertical dashed line). The black line displays the value derived from observations (Evans & Oh 2022).

significant fraction of this radius. We therefore conclude that the elevated dispersion is due to the combined effect of stars bound to the BBH, stars being accelerated by interaction with the BBH (Mapelli et al. 2005) and the Brownian motion of its centre of mass.

The average increase of the velocity dispersion profile in the innermost parsec for models containing BHs indicates the potential

for further validation through observations. Studies estimating the velocity dispersion of the Hyades provide central values as low as 0.3 km s^{-1} (Makarov, Odenkirchen & Urban 2000; Madsen 2003), and upper limits of 0.5 km s^{-1} (Douglas et al. 2019) and 0.8 km s^{-1} (Röser et al. 2011). The *Gaia* data membership selection is often a trade-off between completeness and contamination and, especially for low-mass evolved star clusters, it requires a special case. For example, the data sets from Jerabkova et al. (2021) or Röser et al. (2019), who aimed to detect the extended tidal tails of the Hyades, may not be the ideal for the construction of the velocity dispersion profile.

Since a detailed comparison between theoretical and observed velocity dispersion profiles requires a dedicated membership selection and a thorough understanding of the involved uncertainties, we will leave it to a follow-up focused study. Moreover, the N -body models by Wang & Jerabkova (2021) do not consider primordial binary stars (see discussion in Section 4.2), which might affect the calculated velocity dispersion.

3.6 Dynamical mass estimation

Based on the stellar mass and the velocity dispersion, Oh & Evans (2020) concluded that the Hyades is supervirial and therefore disrupting on an internal crossing time-scale. The measured velocity dispersion within the cluster is commonly used to calculate the dynamical mass of the cluster, as:

$$M_{\text{dyn}} \simeq \frac{10 \langle \sigma_{\text{ID}}^2 \rangle R_{\text{eff}}}{G}. \quad (4)$$

We apply this to our N -body models and compare it to the actual total mass. To be consistent with observations, we defined σ_{ID} as the line-of-sight velocity dispersion of high-mass stars and the effective radius R_{eff} as the radius containing half the number of high-mass

Table 2. Properties of the Hyades models with $150 M_{\odot} \leq M_h \leq 190 M_{\odot}$, for different numbers of BHs in the Hyades at the present day (N_{BH} , column 1): total mass in visible stars (column 2), total mass in high-mass stars (column 3), total mass (column 4), BH mass fraction (column 5), initial mass fraction in O-type stars (column 6), initial total mass (column 7), initial half-mass radius (column 8). The last column reports the percentage of models that evolve into clusters within the mass cut, for the selected N_{BH} . The reported values are the medians of the distributions, while the subscripts and superscripts are the difference from the 16 per cent and 84 per cent percentiles, respectively.

N_{BH}	$M_{\text{vis}} (M_{\odot})$	$M_h (M_{\odot})$	$M_{\text{tot}} (M_{\odot})$	f_{BH}	f_{O}	$M_0 (M_{\odot})$	$r_{h,0} (\text{pc})$	P_{cut}
0 BHs	$233.9^{+21.4}_{-22.1}$	$170.5^{+12.3}_{-15.1}$	$254.0^{+24.4}_{-24.1}$	0	$0.09^{+0.06}_{-0.05}$	$1016.1^{+194.5}_{-16.1}$	$0.98^{+0.99}_{-0.48}$	13.8
1 BHs	$242.5^{+21.0}_{-21.9}$	$170.5^{+15.6}_{-10.7}$	$274.1^{+22.5}_{-25.0}$	$0.04^{+0.02}_{-0.01}$	$0.12^{+0.06}_{-0.06}$	$1201.4^{+200.3}_{-200.6}$	$0.99^{+0.99}_{-0.49}$	13.6
2 BHs	$241.2^{+21.8}_{-22.1}$	$168.1^{+14.5}_{-11.1}$	$280.2^{+22.9}_{-25.4}$	$0.07^{+0.02}_{-0.02}$	$0.15^{+0.05}_{-0.05}$	$1401.4^{+200.3}_{-200.6}$	$1.00^{+0.99}_{-0.50}$	14.2
3 BHs	$242.7^{+27.6}_{-26.2}$	$173.0^{+10.9}_{-18.0}$	$289.6^{+30.8}_{-28.4}$	$0.09^{+0.02}_{-0.01}$	$0.15^{+0.05}_{-0.04}$	$1400.5^{+195.5}_{-197.3}$	$1.96^{+0.03}_{-1.27}$	16.8
4 BHs	$249.3^{+14.2}_{-23.4}$	$167.1^{+14.1}_{-7.2}$	$294.5^{+23.7}_{-22.4}$	$0.11^{+0.02}_{-0.01}$	$0.17^{+0.03}_{-0.04}$	$1400.5^{+195.3}_{-0.2}$	$1.97^{+0.04}_{-0.71}$	27.2
5 BHs	$216.7^{+23.3}_{-8.5}$	$155.6^{+6.0}_{-3.4}$	$281.4^{+18.8}_{-14.2}$	$0.16^{+0.01}_{-0.02}$	$0.18^{+0.02}_{-0.05}$	$1598.5^{+0.3}_{-270.2}$	$1.97^{+0.00}_{-0.02}$	27.2

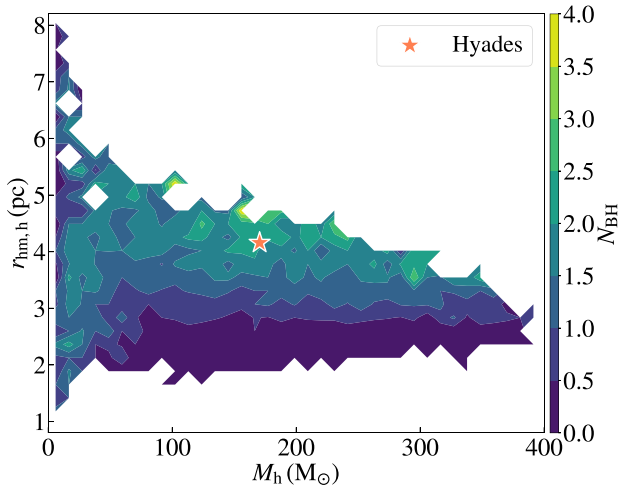


Figure 6. Contour plot of the total mass (M_h) and the half-mass radius ($r_{\text{hm},h}$) of the high-mass stars. The colourmap encodes the local mean number of BHs in that region of the parameter space. The orange star displays the values derived from observations (Evans & Oh 2022).

stars. We find a systematic bias of M_{dyn} overestimating the total mass of the cluster typically by a factor of ~ 1.5 for $N_{\text{BH}} = 0$ and a factor of ~ 2 for $N_{\text{BH}} > 0$. This is due to the presence of energetically unbound stars that are still associated with the cluster, the so-called potential escapers (Fukushige & Heggie 2000), whose fraction increases as the fraction of the initial stars remaining within the cluster decreases (Baumgardt 2001).

In our N -body models, the clusters in the Hyades mass range (within the selected mass cut) typically retain a fraction ~ 0.2 of the initial stars. For these models, the percentage of potential escapers increases from $\lesssim 5$ per cent in the initial conditions to ~ 40 per cent at the present day. The fraction of potential escapers is similar to that found in Claydon et al. (2017) for models initialized with a Kroupa (2001) IMF (between 0.1 and $1 M_{\odot}$) that evolve in a Galactic potential similar to the cusp of a Navarro–Frenk–White (Navarro et al. 1995) potential, the same adopted for the dark matter halo in the MW POTENTIAL2014 (see Section 2.2). If we do not include the potential escapers in the calculation of the dynamical mass (equation 4), we find values that are consistent with the actual total mass of the cluster. We therefore conclude that the high dispersion of Hyades is not because it is dissolving on a crossing time, but because it contains potential escapers and BHs.

3.7 Angular momentum alignment with BBH

The presence of a central BBH may also affect the angular momentum of surrounding stars. In particular, three-body interactions between the central BBH and the surrounding stars can lead to a direct angular momentum transfer. As a consequence, the interacting stars are dragged into corotation, and display angular momentum alignment with the central BBH (Mapelli et al. 2005). This scenario works for BBHs with massive components ($> 50 M_{\odot}$), which are able to affect the angular momentum distribution for a relatively high fraction of stars (Mapelli et al. 2005). We tested this scenario for BBHs with components of lower masses, by considering our models of the Hyades with a central BBH. In this case, stars show isotropic distribution with respect to the central BBH, independently of the distance from the cluster centre. Thus, no signature of angular momentum alignment is found.

3.8 Tidal tails

The relaxation process increases the kinetic energy of stars to velocities higher than the cluster escape velocity, unbinding their orbits into the Galactic field. When this mechanism becomes effective, stellar clusters preferentially lose stars through their Lagrange points (Küpper, MacLeod & Heggie 2008), leading to the formation of the two so-called tidal tails. The members of tidal tails typically exhibit a symmetrical S-shaped distribution as they drift away from the cluster, with overdensities corresponding to the places where escaping stars slow down in their epicyclic motion (Küpper et al. 2010; Küpper, Lane & Heggie 2012).

Until few years ago, tidal tails had mainly been observed in GCs (for example, see Odenkirchen et al. 2003 for the case of Palomar 5), which are more massive, older, and often further from the Galactic plane than OCs. Thanks to the *Gaia* survey, we have now the possibility to unveil such large-scale (up to kpc) structures near OCs dissolving into the Galactic stellar field (for example, Meingast & Alves 2019; Röser et al. 2019). Since the *Gaia* survey only provides radial velocity values for bright stars (Cropper et al. 2018), the search for tidal tail members mostly relies on projected parameters, like the proper motions, which have complex shapes. In this sense, mock observations from N -body models are generally adopted as a reference to recover genuine tail members, and to distinguish them from stellar contaminants (for example, see Jerabkova et al. 2021).

Here, we focus on the impact of the present-day number of BHs on the tidal tail structure. As reported in Table 2, models with a larger number of BHs generally result from the evolution of more massive

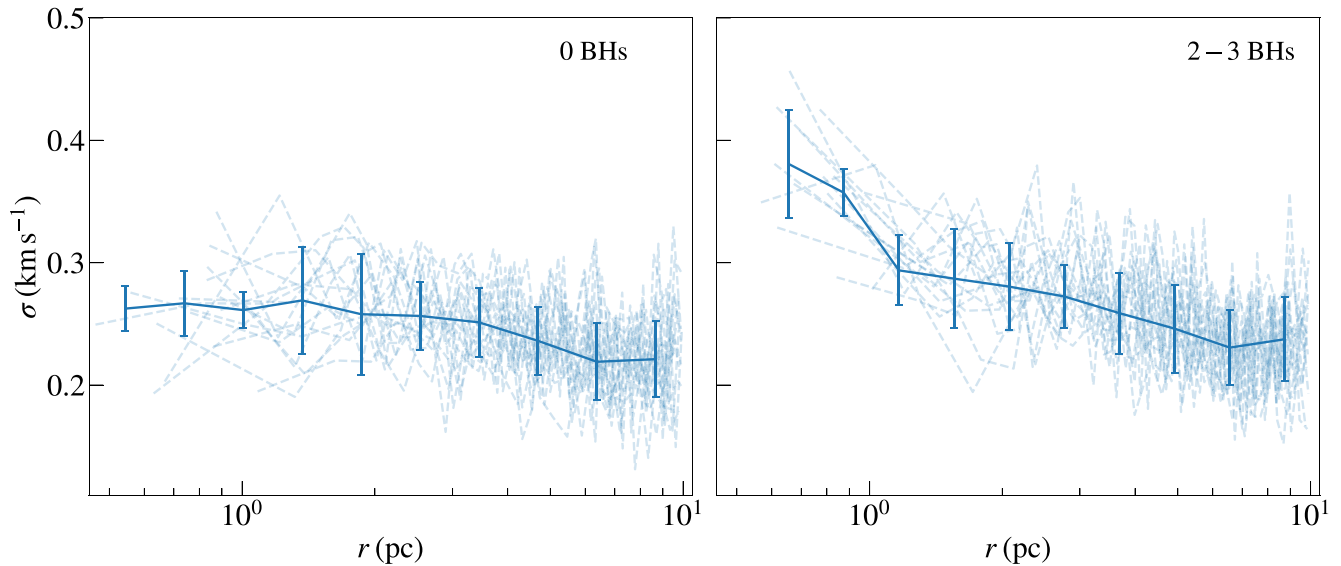


Figure 7. 1D velocity dispersion profiles for 16 models drawn from the cases with $N_{\text{BH}} = 0$ (left-hand panel) and $N_{\text{BH}} = 2-3$ (right-hand panel). The blue dashed lines are the single models. The blue solid line is the median of the distribution at selected radial distances, with the associated errors.

clusters (M_0 is ~ 10 per cent larger), because of the more efficient mass-loss. This may produce a quantifiable impact on the number and density profile of the predicted tails. Fig. 8 shows the number density profiles of the tidal tails from the 16 models with 0 BHs and with 2–3 BHs introduced in Section 3.2. The median profiles and the associated uncertainties are built in the same way as for the density profiles. To reduce the projection effects due to spatial alignment and emphasize the tail structure along the direction of the tail itself, we display the number of stars as a function of the Y_{Galactic} coordinate, rotated so that the V_Y component is aligned with the tail. Also, to obtain a sample that mimics *Gaia* completeness, we consider only stars with magnitude $m_G < 18$ mag. The profiles of models with and without BHs are almost indistinguishable, hinting at a tiny impact from the BH content. This appears in contradiction with the fact that the initial masses of the models with BHs are 50 per cent higher than the models without BHs (see Table 2), while their present-day masses are similar. However, f_0 is also larger for clusters that retain BHs, and this leads to an enhanced mass-loss from winds in the first ~ 50 Myr (see figs 5 and 7 in Wang & Jerabkova 2021). This results in models with $N_{\text{BH}} = 2-3$ having a number of stars in the tails that is only ~ 10 per cent (about 200 stars) larger than those without BHs. The recent mass-loss rates of the two sets of models is comparable. The position of the epicyclic overdensities is not affected by the number of BHs (see also fig. 8 of Wang & Jerabkova 2021).

This result means that the tidal tails of clusters as low-mass as Hyades cannot be used to identify BH-rich progenitors, as was suggested from the modelling of the more massive cluster Pal 5 (Gieles et al. 2021). Future work should show whether tails of more massive OCs are sensitive to the (larger) BH content of the cluster. Also, future studies might specifically target the epicyclic overdensities in more detail and establish their phase-space properties for mode models to provide large statistical grounds. While the current observational data are not sufficient to provide such information, this will likely change with the future *Gaia* data releases and the complementary spectroscopic surveys SDSS-V (Almeida et al. 2023), 4MOST (de Jong et al. 2019), and WEAVE (Dalton et al. 2012).

4 DISCUSSION AND OBSERVATIONAL TESTS

4.1 Dependence of the results on the initial parameters

As shown in Figs 3 and 4, models with 2–3 BHs are favoured to match the observed radial distributions of the Hyades. However, we cannot use the final distributions as posteriors since the initial sampling was done on a rigid grid with fixed number of models at each grid point. In this section, we thus explore how the choice of the initial parameters can affect our results, and if different initial values of M_0 and $r_{\text{hm},0}$ would lead to a different conclusion concerning the consistency of models with 0 BHs with observations.

Fig. 9 shows the percentage distributions of the models that match the observations, as a function of M_0 and $r_{\text{hm},0}$, and for different values of N_{BH} . We define such models as those that lie within the selected mass cut (see Section 2.3) and whose half-mass radius does not differ more than 20 per cent from the observed value. For the considered N_{BH} , we evaluate the percentage of clusters that originate from each $M_0 - r_{\text{hm},0}$ combination. Independently on N_{BH} , models with $M_0 < 1000 M_{\odot}$ can hardly produce Hyades-like clusters. This is also evident from fig. 6 of Wang et al. (2022), which indicates that more massive clusters are needed to reproduce the observed properties.

Most of the models with $N_{\text{BH}} < 3$ lie well within the initial mass range, with lower percentages at the low- and the high-mass end. No clear dependence on the initial radius is found. In contrast, star clusters with 3 BHs mainly result from M_0 and $r_{\text{hm},0}$ at the upper boundary of the parameter distributions. This is mainly due to the larger number of massive progenitors, which enhance the cluster mass-loss, as already pointed out in Section 3.4. At the same time, models with larger radii retain more BHs (fewer dynamical interactions) and they therefore need to be more massive.

Our analysis suggests that more massive and extended initial conditions may produce Hyades-like clusters. However, these clusters are likely to host $N_{\text{BH}} \geq 3$. Thus, a more extensive exploration of the initial parameter space is expected to strengthen the conclusion that a fraction of BHs needs to be retained within the cluster to match the observed properties of the Hyades. Furthermore, Fig. 5

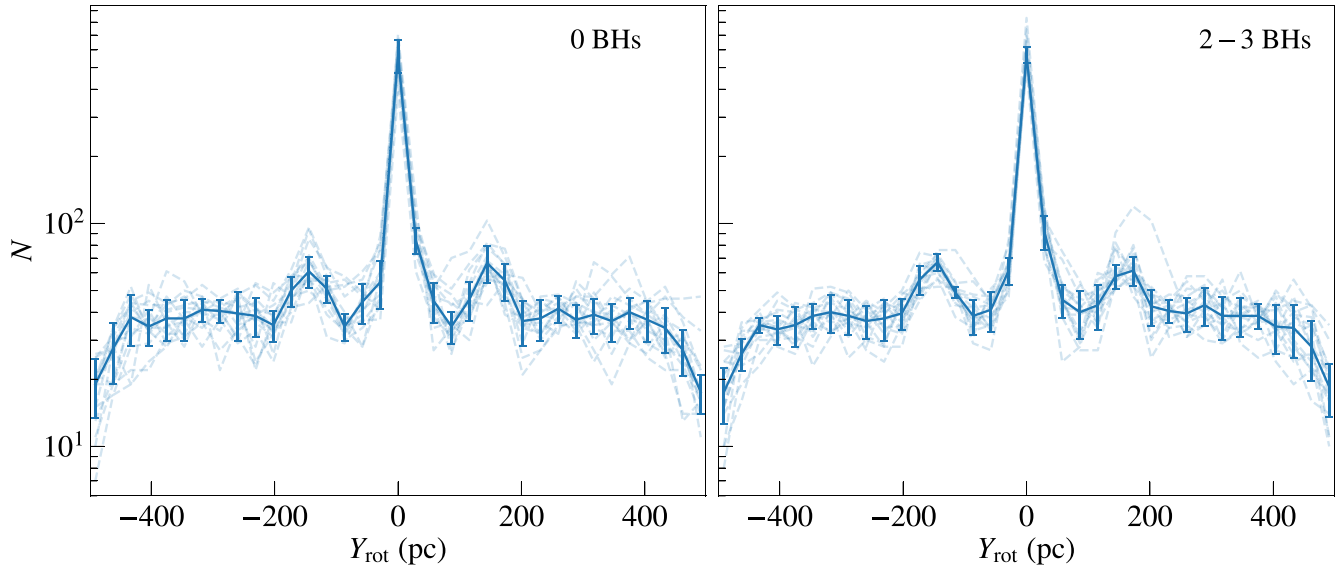


Figure 8. Tidal tail profiles for 16 models drawn from the cases with $N_{\text{BH}} = 0$ (left-hand panel) and $N_{\text{BH}} = 2-3$ (right-hand panel). The Y Galactic coordinate is rotated, so that the V_Y component is aligned with the tail. The profiles are obtained from the N -body models by considering all the visible stars with magnitude $m_G < 18$.

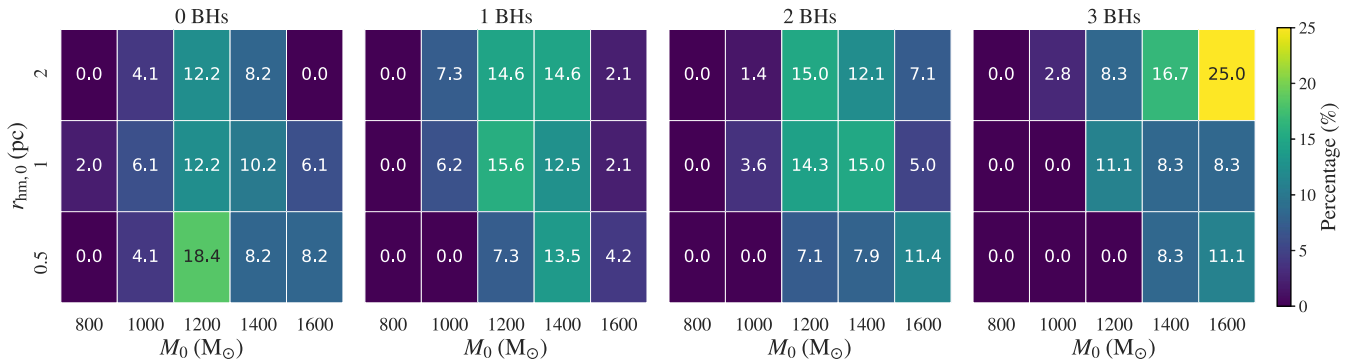


Figure 9. Percentage distributions of models that match the observations as a function of M_0 and $r_{\text{hm},0}$, for different numbers of BHs in the Hyades at the present day. Here, we define the models that match the observations as those that lie within the selected mass cut (see Section 2.3) and whose half-mass radius does not differ more than 20 per cent from the observed value.

indicates that models with no retained BHs end up too small, independently on their initial radius. Therefore, clusters with larger initial radii and no retained BHs are expected to shrink and lose mass at a constant density (Hénon 1965), as also found for the case of Palomar 5 (see Gieles et al. 2021). As a consequence, there is no hint that, by extending the range of initial conditions, we will find different conclusions on the consistency of models with no BHs with observations.

4.2 Possible effect of primordial binaries

The N -body models considered for this work do not contain primordial binaries, but observations find that young star clusters have high binaries fractions, especially among massive stars (Sana et al. 2012; Moe & Di Stefano 2017). Here we discuss the possible effect of primordial binaries on the structure of clusters and, in particular, whether there may be a degeneracy with the effect of BHs. Wang et al. (2022) investigated the impact of different mass-dependent primordial binary fractions on the dynamical evolution of star clusters with N -body simulations. Their results show that

massive primordial binaries (component masses $> 5 M_{\odot}$) dominate over low-mass binaries and that in the presence of massive binaries the evolution of the core and half-mass radius is insensitive to the binary fraction among low-mass stars (see fig. 5 in Wang et al. 2022). Models with 100 per cent binaries have a ~ 10 per cent larger half-mass radius than models without binaries. This difference is less than the difference we find between clusters with and without BHs.

However, the model clusters of Wang et al. (2022) are more massive ($N \sim 10^5$), so they all contain some BHs. Hurley (2007) presents N -body models of clusters without BHs and with modest binary fractions (5 per cent and 10 per cent). The BH natal kicks are larger in his model and BH retention is therefore rare. He finds that the binary fraction does not affect the evolution of the core and half-mass radius. Giersz & Heggie (2011) find from Monte Carlo models of 47 Tucanae that the evolution of the half-mass radius is not affected by primordial binaries. Hurley (2007) showed that when two BHs are retained, the effect of the BBH that inevitably forms on the observed core and half-mass radius is far larger than the primordial binaries. In particular, his fig. 6 shows that the model with a BBH has a central surface density that is a factor of ~ 4 lower than

models with binaries and without BBH. Given the modest binary fraction of Hyades (~ 20 per cent; Kopytova et al. 2016; Evans & Oh 2022; Brandner, Calissendorff & Kopytova 2023), we therefore conclude that it is unlikely that primordial binaries have the same effect on the density profile as BHs. However, it would be interesting to verify this.

In conclusion, we recognize that the presence of primordial binaries play a crucial role on the long-term evolution of a cluster like the Hyades. However, a detailed characterization of the primordial binary impact on the cluster present-day structure, as well as a complete disentanglement of their observational signatures from those left by BHs, requires a more in-depth study. For this reason, we will explore it in a future work.

4.3 BH companions

Three-body interactions within a stellar cluster strongly favour the formation of binary systems, mainly composed of the most massive objects (Heggie 1975). As a consequence, BHs tend to form binaries preferentially with other BHs, and when in binaries with a lower mass stellar companion, they rapidly exchange the companion for another BH (Hills & Fullerton 1980). In general, the result is a growing BBH population in the cluster core (Portegies Zwart & McMillan 2000). In OCs, however, given the limited number of BHs by the initial low number of massive stars, a non-negligible fraction of BH-star binary systems may form and survive.

Binary stars in dynamically active clusters are expected to display semimajor axis distributions that depend on the cluster properties. Soft binaries (with binding energy lower than the average cluster kinetic energy) are easily disrupted by any strong encounter with another passing star or binary (Heggie 1975). The upper limit for the semimajor axis is thus given by the hard–soft boundary of the cluster:

$$a_{\max} = \frac{Gm_1m_2}{2\langle m\sigma^2 \rangle}, \quad (5)$$

where $m_{1,2}$ are the masses of the binary components, and $E_b = \langle m\sigma^2 \rangle$ is the hard–soft boundary (Heggie 1975). For an OC with $\sigma \approx 0.5 \text{ km s}^{-1}$, the upper limit for a binary composed of a black-hole ($m_1 = 10 M_\odot$) and a star ($m_2 = 1 M_\odot$) is of the order of $a_{\max} \sim 10^{-1} \text{ pc}$.

When a hard binary is formed, it becomes further tightly bound through dynamical encounters with other cluster members (Heggie 1975; Goodman 1984; Kulkarni, Hut & McMillan 1993; Sigurdsson & Phinney 1993). Each encounter causes the binary to recoil, until the binary becomes so tight that the recoil is energetic enough to kick it out from the cluster. For this, the lower limit a_{\min} can be assumed to be the semimajor axis at which the binary that produces a recoil equal to the escape velocity v_{esc} . Following Antonini & Rasio (2016):

$$a_{\min} = 0.2 \frac{Gm_1m_2}{v_{\text{esc}}^2} \frac{m_3^2}{m_{12}^2m_{123}}, \quad (6)$$

where $m_3 = \langle m \rangle$, $m_{12} = m_1 + m_2$, and $m_{123} = m_1 + m_2 + m_3$. For an open cluster with $v_{\text{esc}} \approx 0.5 \text{ km s}^{-1}$, $m_1 = m_2 = 10 M_\odot$, and $m_3 = 0.5 M_\odot$, we obtain $a_{\min} \sim 10^{-5} \text{ pc}$ (2 AU). For a BH-star binary system ($m_2 = 1 M_\odot$), $a_{\min} \sim 10^{-4} \text{ pc}$.

BHs in our N -body models, as expected, show a tendency to dynamically couple with other objects, and form binary and triple systems. When $N_{\text{BH}} > 0$, only 6 per cent of the BHs are not bound in binary or multiple systems. Even in models where only 1 BH is present, the single BH tends to form binaries with (mainly) stars or

other remnants (white dwarfs or neutron stars). Fig. 10 shows the distribution of semimajor axes and periods for binaries and triple systems of clusters with N_{BH} ranging from 1 to 4. Independently of N_{BH} , most of the binaries display semimajor axes from 10^{-5} to 10^{-1} pc , consistently with our approximate calculation. When more than 1 BH is present, dynamical interactions tend to favour the formation of BBHs. As reported in Table 3, the fraction of BBHs represents by far the largest fraction of binary systems hosting BHs if more than 1 BHs is present.

4.4 Binary candidates in the Hyades

In this section, we present a search for possible massive companions to main sequence stars in the Hyades. We identify binary candidates by searching for members with enhanced *Gaia* astrometric and spectroscopic errors (following Belokurov et al. 2020; Penoyre et al. 2020, and Andrew et al. 2022).

4.4.1 Selecting cluster members

We start with all *Gaia* DR3 sources with $\varpi > 5 \text{ mas}$, RA between 62 and 72 degrees, Dec between 13 and 21 and *RUWE*, which stands for renormalized unit-weight error, greater than 0 (effectively enforcing a reasonable 5-parameter astrometric solution) – giving 5640 sources as shown in Fig. 11. We also apply an apparent G-band magnitude cut of $m_G < 15$ above which the astrometric accuracy of *Gaia* starts to degrade rapidly due to Poisson noise. Analysis beyond this magnitude is eminently possible, but for such a nearby population of stars this cut excludes a minority of the cluster (even more so the likely binary systems, as binary fraction increases with mass) and means that *Gaia* should have a near constant ($\sim 0.2 \text{ mas}$, Lindgren et al. 2021) precision per observation and thus allows uncomplicated comparison of sources.

To select cluster members we use the position, proper motion, and parallax to construct an (unnormalized) simple membership probability:

$$p_{\text{member}} = e^{-\sum_x \left(\frac{x-x_0}{\sigma_x} \right)^2}, \quad (7)$$

where

$$\sigma_x^2 = \sigma_x^2 + \sigma_{\text{AEN}}^2 + \sigma_{x_0}^2 \quad (8)$$

with x denoting each of the parameters of RA, Dec, $\mu_{RA^*} (= \mu_{RA} \cos(\text{Dec}))$, μ_{Dec} and ϖ . σ_x is the reported uncertainty on each parameter in the *Gaia* catalogue and σ_{AEN} is the `astrometric_excess_noise` (AEN) of the fit. x_0 and σ_{x_0} are the assumed values and spread of values expected for the cluster as listed in Table 4. The inclusion of the AEN ensures that potentially interesting binaries, which may have a significantly larger spread in their observed values and thus fall outside of the expected variance of the cluster, are not selected against.

The value of p_{member} for stars in the field is shown in Fig. 12 from which we choose a critical value of $\log_{10}(p_{\text{member}}) = -1.75$ giving 229 members which can be seen and identified on the Hertzsprung–Russell diagram shown in Fig. 13.

4.4.2 Astrometric and spectroscopic noise

Following the method introduced in Andrew et al. (2022), we can use the astrometric and spectroscopic noise associated with the measurements in the *Gaia* source catalogue (which assumes every

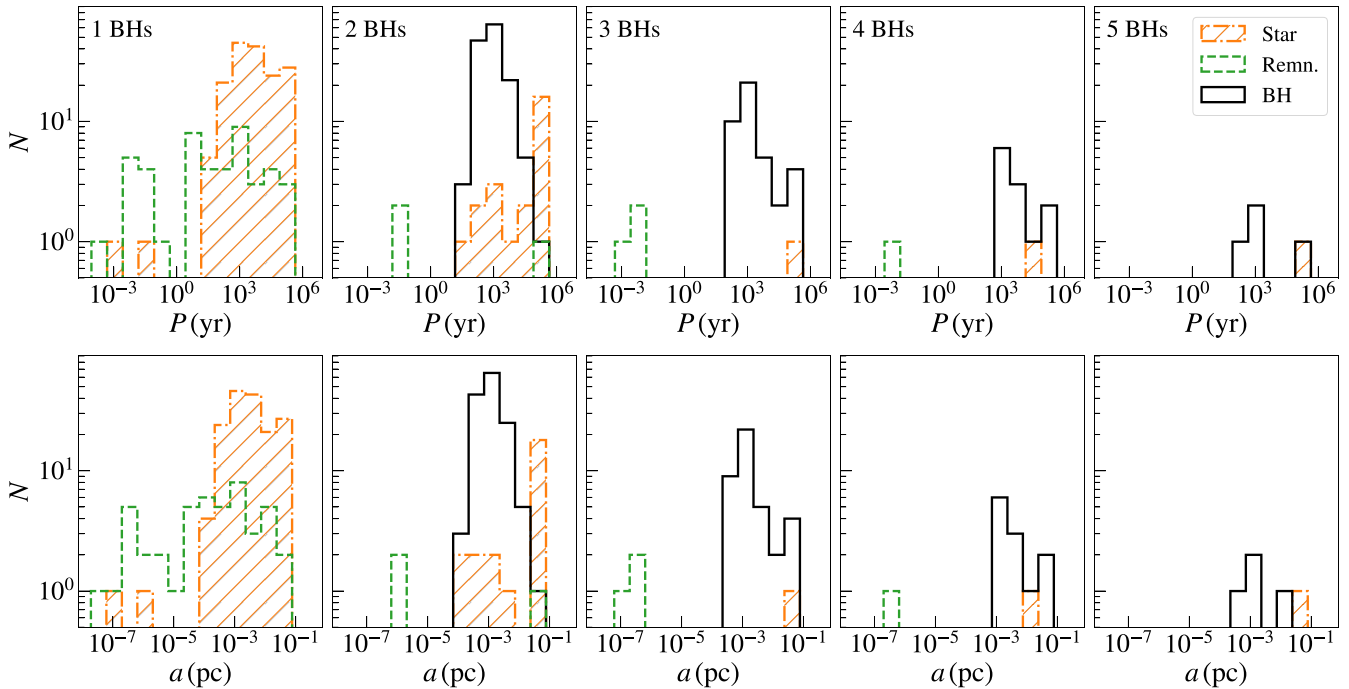


Figure 10. Distributions of periods (upper panels) and semimajor axes (lower panels) of the binary and triple systems hosting BHs, for N -body models with different N_{BH} . We distinguish between different types of BH companions: stars (orange dash-dot line, hatched area), white dwarfs or neutron stars (green dashed line), and BHs (black).

Table 3. Fractions of binary systems hosting BHs, for different N_{BH} (column 1). We distinguish between different types of BH companions: stars (column 2), white dwarfs or neutron stars (column 3), and BHs (column 4).

N_{BH}	$f_{\text{BH-Star}}$	$f_{\text{BH-Remn.}}$	$f_{\text{BH-BH}}$
1 BHs	0.78	0.22	0.0
2 BHs	0.15	0.02	0.83
3 BHs	0.02	0.07	0.91
4 BHs	0.07	0.07	0.86
5 BHs	0.2	0.0	0.8

star is single) to identify and characterize binary systems. This is possible for binaries with periods from days to years, as these can show significant deviations from expected single-body motion. As *Gaia* takes many high-precision measurements, the discrepancy between the expected and observed error behaviour is predictable and, as we will do here, can be used to estimate periods, mass ratios, and companion masses.

The first step is to select systems with significant excess noise. For astrometry, we can use a property directly recorded in the catalogue, named *RUWE*. This is equal to the square root of the reduced chi-squared of the astrometric fit and should, for well-behaved observations, give values clustered around 1. Values significantly above 1 suggest that either the model is insufficient, the error is underestimated, or there are one or more significant outlying data points. Given that binary systems are ubiquitous (a simple rule-of-thumb is that around half of most samples of sources host more than one star, see for example Offner et al. 2022), these will be the most common cause of excess error, especially in nearby well-characterized systems outside of very dense fields.

It is possible to compute a reduced-chi-squared for any quantity where we know the observed variance, expected precision, and the degrees of freedom – and thus we can find the *RUWE* associated with spectroscopic measurements as well. To do this, we need to estimate the observational measurement error, which we do as a function of the stars’ magnitude and colour (as detailed in Andrew et al. 2022) giving $\sigma_{\text{spec}}(m_G, m_{BP} - m_{RP})$, the uncertainty expected for a single measurement for each source. Thus we can construct a spectroscopic renormalized unit-weight error, which we’ll call *RUWE*_{spec} to use alongside the astrometric which we’ll denote as *RUWE*_{ast}. These values are shown for Hyades candidate members in Fig. 14.

Only a minority of *Gaia* sources have radial-velocity observations, which can be missing because sources are too bright ($m_G \lesssim 4$, as seen at the top of the HR diagram), too dim ($m_G \gtrsim 14$, as seen at the bottom), in too dense neighbourhoods, or if they are double-lined (with visible absorption lines in more than one of a multiple system, as may be the case with some likely multiple stars above the main-sequence). We use only systems with `rv_method_used = 1` as only these are easily invertible to give binary properties (Andrew et al. 2022 for more details).

The particular value at which *RUWE* is deemed significantly must be decided pragmatically, and we adopt the values from Andrew et al. (2022) of *RUWE*_{ast} > 1.25 and *RUWE*_{spec} > 2, where the higher criteria for spectroscopic measurements stems from the smaller number of measurements per star and thus the wider spread in *RUWE*. We select sources satisfying both of these criteria as candidate Hyades binaries, giving 56 systems. There are some sources that exceed one of these criteria and not the other, and these are interesting potential candidates, but they cannot be used for the next step in the analysis. Using both (generally independent) checks should significantly reduce our number of false positives. It is worth noting that radial-velocity signals are largest for short-period orbits, whereas astrometric signals are largest for systems whose periods match the

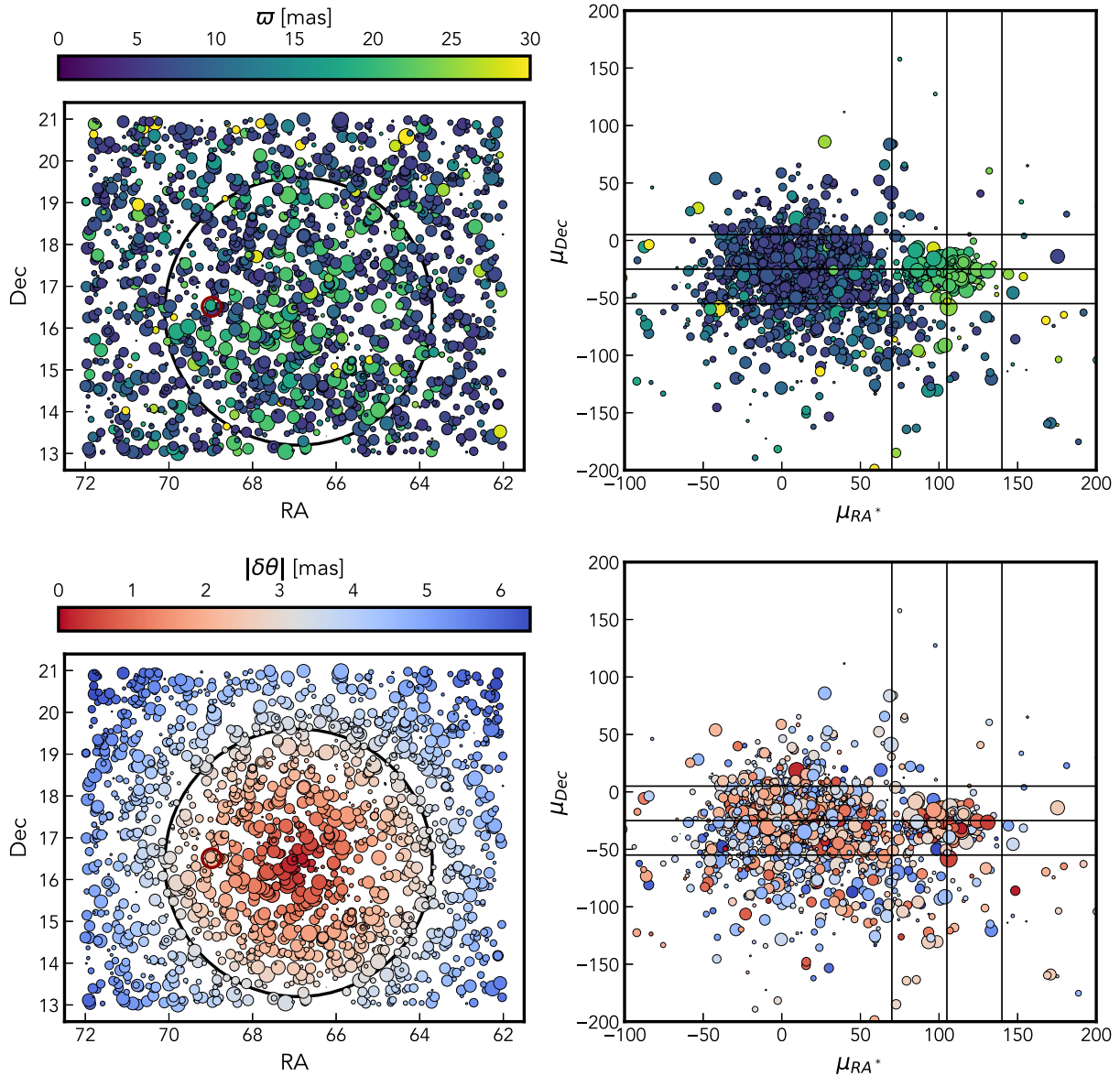


Figure 11. Position on sky (left-hand panel) and proper motion (right-hand panel) of sources in the field of the Hyades (with $\varpi > 5$ mas). We show the parallax (top row) and angular offset from the centre of the cluster (bottom row). Aldebaran, a foreground star too bright for *Gaia*, is shown as a red open circle. The size of each point is set by their apparent magnitude and only sources with $m_G < 15$ are shown (see Fig. 13 for reference). We show an angular offset of 3.2 mas (black circle, left-hand panel) and lines denoting $\mu_{RA^*} = 105 \pm 35$ mas yr $^{-1}$ from this (black vertical lines, right-hand panel) and $\mu_{Dec} = -25 \pm 30$ mas yr $^{-1}$ (black horizontal lines, right-hand panel).

Table 4. Values for ϖ , RA, Dec, μ_{RA^*} , μ_{Dec} , and their reported uncertainty in the *Gaia* catalogue.

	ϖ	RA	Dec	μ_{RA^*}	μ_{Dec}
x_0	22	66.9	16.4	105	-25
σ_{x_0}	7	3.2	3.2	35	30

time baseline of the survey (34 months for *Gaia* DR3). This both tells us about which systems we might miss or might meet one criterion and not the other. It also gives the explanation for one of the largest sources of contaminants in this process: triples (or higher multiples) where each significant excess noise comes from a different orbit and thus the two cannot be easily combined or compared.

If we know the *RUWE* and the measurement error, and assume that all excess noise comes from the contribution of the binary we can invert to find specifically the contribution of the binary:

$$\sigma_{b,\text{spec}} = \sqrt{RUWE_{\text{spec}}^2 - 1} \cdot \sigma_{\text{spec}}(m_G, m_{BP} - m_{RP}). \quad (9)$$

and

$$\sigma_{b,\text{ast}} = 2\sqrt{RUWE_{\text{ast}}^2 - 1} \cdot \sigma_{\text{ast}}(m_G), \quad (10)$$

where the factor of 2 comes from the fact that *Gaia* takes 1D measurements of the stars 2D position.

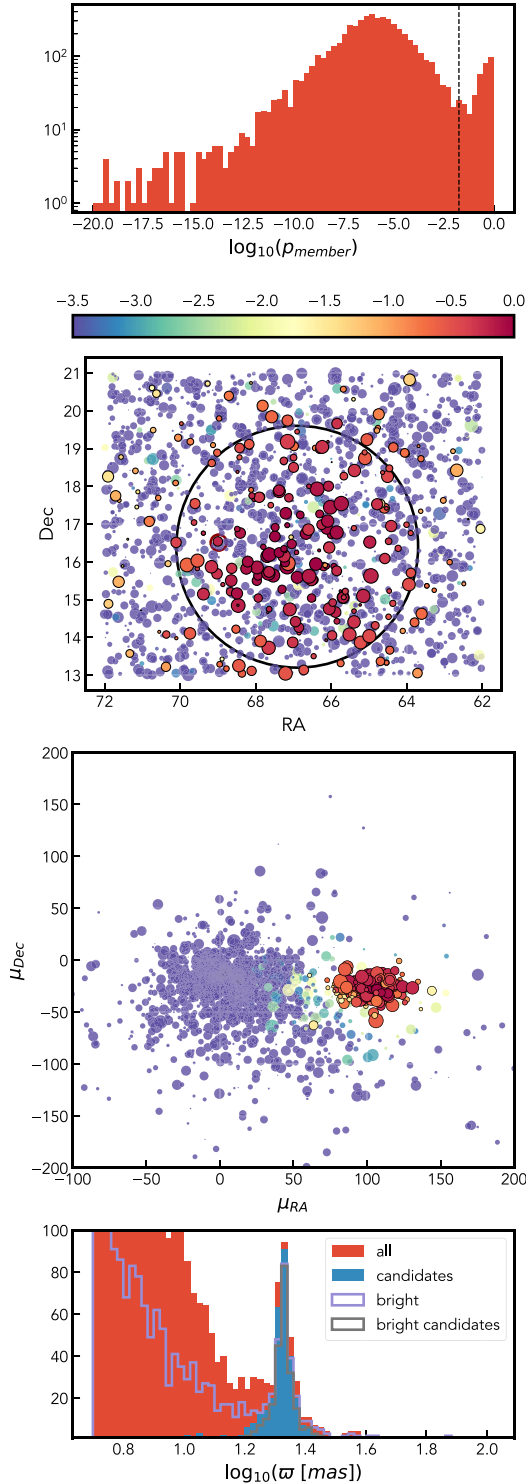


Figure 12. Cluster membership probability for stars in the Hyades field based on equation (7). We show the distribution for all stars (top) and, based on this, the cut at $\log_{10}(p_{\text{member}}) = -1.75$ (vertical dashed line). The middle two panels show the position and proper motion distribution (similar to Fig. 11) coloured by $\log_{10}(p_{\text{member}})$. Stars with values greater than -1.75 are shown with black outlines. The bottom panel shows the parallax distribution of all stars in our field and our candidates.

4.4.3 Binary properties from excess error

The contributions in equations (9) and (10) can be mapped back to the properties of the binary and inverted to give the period and (after estimating the mass of the primary) the mass of the companion, as detailed in Andrew et al. (2022). For binary periods less than or equal to the time baseline of the survey the period is approximately:

$$P = \frac{2\pi A}{\varpi} \frac{\sigma_{b,\text{ast}}}{\sigma_{b,\text{spec}}}, \quad (11)$$

and the mass ratio follows:

$$q^3 - \alpha q^2 - 2\alpha q - \alpha = 0, \quad (12)$$

where

$$\alpha = \frac{A}{GM\varpi} \sigma_{b,\text{spec}}^2 \sigma_{b,\text{ast}} \quad (13)$$

and $A = 1$ AU. M is the mass of the primary star which can be estimated via:

$$M = 10^{0.0725(4.76 - m_G)}, \quad (14)$$

where m_G is the absolute magnitude of the star (Pittordis & Sutherland 2019). This is only strictly relevant for main-sequence stars – but all evolved systems in the Hyades are too bright for *Gaia* spectroscopic measurements and thus will not be included in later analysis (with the exception of white dwarfs, which are too dim).

These equations assume the companion has negligible luminosity of its own. If this assumption does not hold then the period is slightly overestimated and the mass ratio (and companion mass) are slightly underestimated (see fig. 3 of Andrew et al. 2022 for more detailed behaviour). The inferred properties of all 56 systems are shown in Fig. 15 and recorded in Table 5.

There are some simple consistency checks we can apply to these results. Primarily we know that astrometric measurements should only be discerning for binaries with periods from months to decades (Penoyre, Belokurov & Evans 2022) – thus any deep blue or deep red points are likely spurious solutions – though there are only a handful that have erroneous seeming periods.

As we are searching for significant-mass BHs, we focus on the sources with the highest values of q and M_c , but we should be careful as this is equivalent to selecting those with the largest errors and thus possibly those most likely to truly be erroneous (rather than caused by a binary). For example, the highest mass ratio ($q > 1$) sources are amongst the dimmest and thus least reliably measured in the sample – these could be physical, most likely white dwarf companions – but could also be random error. The brighter stars that show evidence of companions have relatively modest properties – mass ratios below 1 and companion masses significantly below those of a clear BH companion.

Given the period constraints on binaries including BHs present in the simulations, as presented in Fig. 10, it is not shocking that we do not find any likely companions. We certainly cannot rule out that these or other stars in the Hyades might have massive compact companions on smaller or wider orbits that *Gaia* would be insensitive to. Instead, we are pleased to be able to present a list of candidate binaries whose companions are most likely similar main-sequence stars or white dwarfs.

Stars with massive companions may still be identifiable via their velocity offset. The orbital velocity of a $1.5 M_\odot$ star in a binary with a companion of $15 M_\odot$ and a period of $10^3(10^4)$ yr has an orbital velocity of $\sim 7(3)$ km s $^{-1}$. Searching for these systems from velocity offsets is beyond the scope of this work but is an interesting avenue for future exploration.

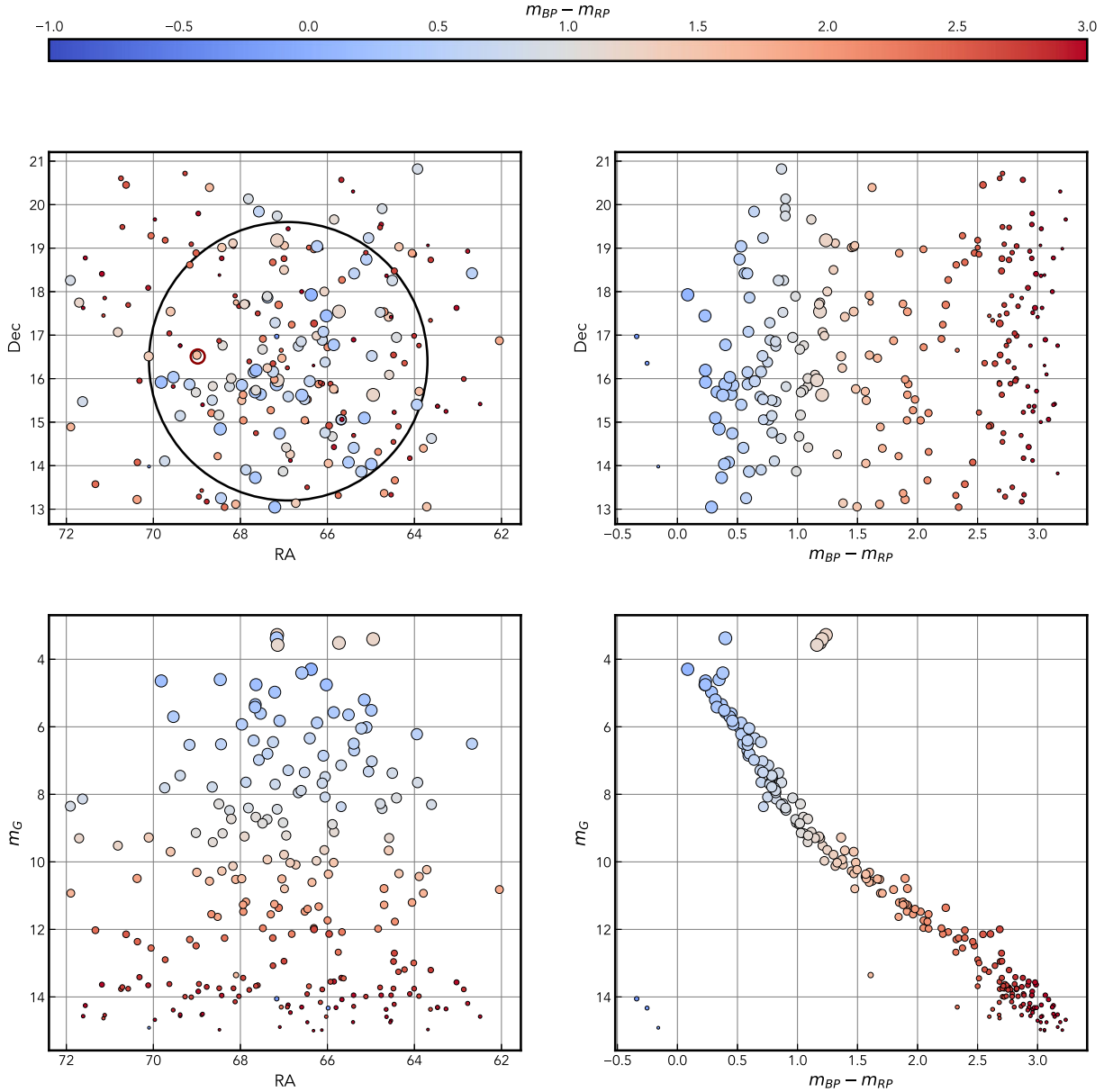


Figure 13. Sky maps and colour–magnitude diagrams for the Hyades candidates, coloured by *Gaia* colour.

4.5 Implications for gravitational waves

Given the vicinity of the Hyades, it is interesting to ask the question whether a BBH in the Hyades would be observable as a continuous gravitational wave source with ongoing or future experiments. Let us therefore adopt a BBH with component masses of $m_1 = m_2 = 10 M_\odot$, an average stellar mass of $\langle m \rangle = 0.5 M_\odot$ and an escape velocity from the centre of the cluster of $v_{\text{esc}} = 0.5 \text{ km s}^{-1}$. Then we assume that the semimajor axis is $a = a_{\text{min}} = 2 \text{ AU}$, i.e. the minimum before it is ejected in an interaction with a star (equation 4.3). This is the most optimistic scenario, because it results in the smallest a , but since the interaction time between stars and the BBH goes as $1/a$, a BBH spends a relatively long time at this final, high binding energy. An estimate of the absolute duration can be obtained from the required energy generation rate (Antonini & Gieles 2020b), from which we find $\sim 5 \text{ Gyr}$. Because this is much longer than the Hyades’

age, it is a reasonable assumption that a putative BBH is near this highest energy state. For the adopted parameters, $a_{\text{min}} \simeq 2 \text{ AU}$. For a typical eccentricity of ~ 0.7 , the peak frequency ($\sim 5 \times 10^{-4} \text{ mHz}$, equation (37) in Wen 2003), i.e. below the lower frequency cut-off of LISA ($\sim 0.1 \text{ mHz}$) and the orbital period of $\sim 0.7 \text{ yr}$ is comparable to the maximum period that can be found by LISA ($\sim 0.7 \text{ yr}$; Chen & Amaro-Seoane 2017). Only for eccentricities $\gtrsim 0.99$ (2 percent probability for a thermal distribution) the peak frequency is $\gtrsim 0.1 \text{ mHz}$. BH masses ($\gtrsim 30 M_\odot$) result in orbital periods comfortably in the regime that LISA could detect ($\lesssim 0.08 \text{ yr}$), but such high masses are extremely unlikely given the high metallicity of the Hyades.

Because of the low frequency, we consider now whether a BBH in Hyades is observable with the Pulsar Timing Array (PTA). Jenet, Creighton & Lommen (2005) show that a BBH at a minimum

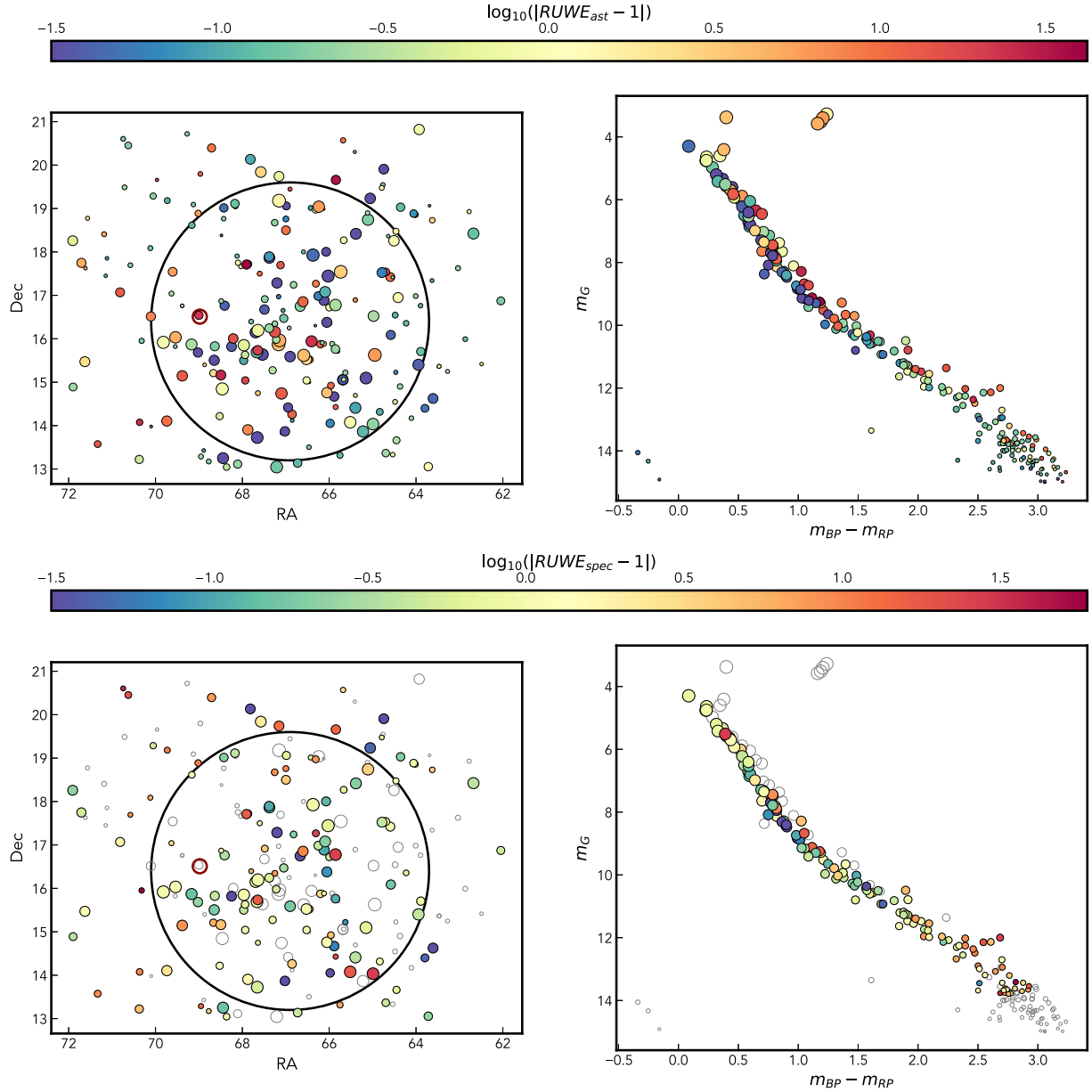


Figure 14. Hyades candidates coloured by astrometric (top) and spectroscopic (bottom) renormalized-unit-weight-error ($RUWE$). Values significantly above 1 suggest that the system has an extra source of noise, most ubiquitously a binary companion. Many sources do not have radial velocity measurements in the *Gaia* source catalogue, and these are denoted with empty grey circles in the bottom plot.

distance to the sightline to a millisecond pulsar (MSP) of 0.03 pc (~ 3 arcmin for the Hyades' distance) causes a time-of-arrival fluctuation of 0.2–2 ns, potentially observable (van Straten et al. 2001). Unfortunately, the nearest MSP in projection is PSR J0407+1607 at 5.5 deg.² If the BBH was recently ejected, it may be close to a MSP in projection, but the maximum distance a BBH could have travelled is ~ 1 deg (Section 3.2) and there are only 4 pulsars within a distance of 10 deg, so this is unlikely as well. In conclusion, it is unlikely that

²ATNF Pulsar Catalogue by R.N. Manchester et al., at <http://www.atnf.csiro.au/research/pulsar/psrcat>

(continuous) gravitational waves from a BBH in or near the Hyades will be found.

4.6 Gravitational microlensing

Because of the vicinity of the Hyades, BHs have relatively large Einstein angles and we may detect a BH or a BBH through microlensing. For a BH mass of $10M_{\odot}$ at a distance of 45 pc and a source at 5 kpc, the Einstein angle is $\theta_E \simeq 40$ mas. Assuming that background stars in the Galaxy are distant enough to act as a source, we find from the *Gaia* catalogue that the on-sky density of background sources is $\Sigma_S \simeq 10^{-9} \text{mas}^{-2}$. The Hyades moves with an on-sky velocity of $v_H \simeq 100 \text{mas yr}^{-1}$ relative to the field

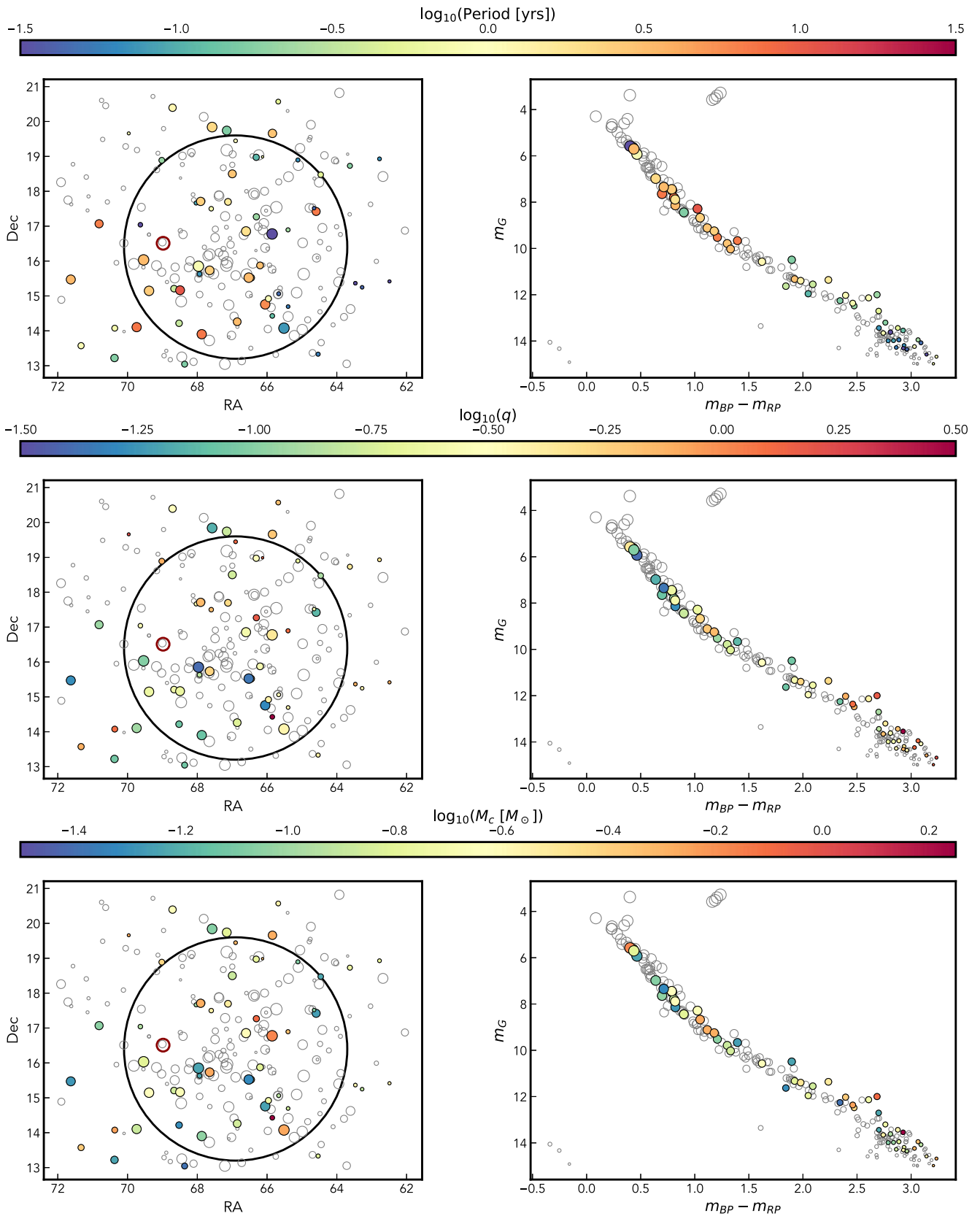


Figure 15. Periods, mass ratios (q), and companion masses (M_c) of Hyades candidates inferred from astrometric and spectroscopic $RUWE$. Only sources with significantly high $RUWE$ in both measurements are included here, and all others are shown with empty grey circles.

Table 5. Candidate binaries in the Hyades with significant astrometric and spectroscopic excess noise. RA and Dec are in degrees-sigmaspec and M_c are expressed in the appropriate combinations of mas, yr, and M_\odot .

sourceid	RA	Dec	parallax	pmra	pmdec	mg	bppp	RUEast	sigmastab	RUEspec	sigmaspec	P	q	M_c
3313842529024545664	65.85493019594335	16.777147465731876	20.795046	106.97092	-26.247469	5.573977	0.40038252	1.2823561	0.41557395	27.358295	23.794285	0.025030272	0.44117424	0.6805129
3311000119668435200	65.515180253603637	14.077103275227195	22.026937	113.774475	-21.321016	5.6442456	0.42680836	1.8872856	0.7889371	19.065733	14.198232	0.075180255	0.3714967	0.5546593
3309990523179108480	69.53972879902068	16.03321720295417	17.820915	84.96662	-8.793861	5.7026787	0.4365778	5.6922646	2.4559207	2.1845562	1.2523471	3.2795131	0.09720816	0.15520167
3312637842237882880	67.96612153925633	15.8514711350184573	21.005054	99.49563	-34.32999	5.928877	0.46518755	1.5450443	0.47656766	2.0089986	0.8186548	0.82594234	0.03999896	0.057937805
144130516816579200	67.57532736919829	19.84041406012967	19.89243	86.11872	-26.106121	6.9827037	0.6383934	3.7624655	1.3966988	3.2055814	0.9599861	2.179701	0.069570266	0.08619921
3312751882209460864	66.52490368958763	15.524230392191061	23.521027	124.196014	-25.313429	7.3494782	0.7129674	3.4419775	1.343747	2.0151875	0.5174881	3.2901115	0.044089917	0.04835587
33094937200191304576	69.38373895275495	15.146378860785259	25.64366	101.49229	-18.512648	7.4436464	0.7864218	4.709577	1.9607697	2.121658	2.558703	2.6238859	0.2289321	0.23954499
331151233797884416	66.05246947657736	14.758157583423541	20.856197	110.226265	-12.401878	7.4817166	0.7890749	4.709577	1.9607697	2.121658	0.4972577	5.634556	0.05053243	0.056626927
3307815006281475200	67.87268564180225	13.903399057854472	20.276747	86.607285	-6.108541	7.643193	0.69734	8.31893	3.525965	2.614277	0.7415865	6.9882374	0.083096355	0.09157219
3309170875916905856	69.73925748852255	14.105477042258816	18.390837	91.53597	-20.422842	7.8071556	0.80762196	10.741918	4.6240096	3.6913257	1.0178571	7.361735	0.118229695	0.1313378
3313743710417140864	66.60303643900508	16.853180488088583	26.757921	95.673996	-38.761845	7.8861456	0.81799173	12.058122	5.1952686	10.748748	3.0819666	1.8774892	0.25809193	0.24698886
330900602007842048	67.62700947833584	15.471931785895292	20.5006	87.325676	-25.352728	8.138844	0.8205805	3.2997699	1.3771452	2.1922784	3.40549	0.052342582	0.052890003	
3309540170088830464	68.494384992386096	15.16352719505778	20.641268	108.03673	-33.110138	8.2856655	1.0252385	27.214418	11.50729	5.577302	1.5087116	11.012355	0.22136614	0.2177251
48061409893621248	67.1555527872302	19.74051990049017	20.810343	102.9064	-38.101357	8.441752	0.89888763	1.6440603	0.53488284	14.239208	4.5749774	0.16743268	0.16246925	0.15522723
3312631623125272448	67.64578394363194	15.733880135447295	17.485168	100.58648	-25.256905	8.67361	1.0493889	21.024082	7.626148	18.202843	5.276344	2.4634974	0.55225676	0.54067534
48197783694869760	65.84566930782594	19.658531350570186	21.598646	97.3178	-37.780178	9.1158905	1.1155329	34.355576	10.966481	16.315971	5.2403026	2.887581	0.62754923	0.52858657
33141512512739592832	67.9051025367819	17.70963694563987	28.507998	98.723816	-22.038061	9.247976	1.1795635	43.27126	13.478946	17.99285	5.767014	2.443363	0.70073265	0.5220939
34062163835235959936	70.81594857548913	17.068982088574	22.40773	84.4349	-41.66873	9.519791	1.2086744	14.337425	4.4526625	2.7862427	0.90990114	6.508449	0.11398687	0.08850268
47319858019739264	64.59216618931373	17.421415275740294	23.752161	104.46378	-50.567753	9.66315	1.3945608	10.326841	3.221443	2.0533266	0.5846881	6.9130993	0.07403989	0.054991435
33144840494059409408	66.99617799986078	18.500100518411095	19.760468	108.59516	-40.885216	9.7873955	1.2999792	10.631993	3.3175225	4.8615503	1.7125669	2.9215875	0.1696449	0.13192531
3310876802567157248	66.85605547720428	14.260578556388577	20.42228	102.45836	-19.95602	10.026131	1.33076	12.669773	3.9585905	4.7959375	1.7974386	3.2138977	0.18906817	0.13960828
3308127405023027328	70.3740966937844	13.221124178946916	22.662909	99.23287	-18.63009	10.491406	1.8964214	1.4050351	0.29435474	5.7457695	2.2721488	0.1703603	0.08793274	0.057852447
3410898202818634624	68.70917414686971	20.394419352148518	18.76046	110.18581	-22.617853	10.571909	1.6212931	9.876004	2.8892152	8.526632	3.900182	1.1767963	0.32126498	0.2233311
3313526556869575296	66.20070596676636	15.874649203665436	20.678333	100.34452	-12.269188	11.324224	1.9229269	12.951795	4.8260064	3.9638534	2.295628	3.0298467	0.2657315	0.15727599
3314185129975960448	67.120038862642493	17.695791947186837	20.918434	109.48695	-44.22729	11.360385	2.2351828	15.092351	5.5574145	8.521062	4.8796754	1.6225665	0.52000636	0.3046414
3312751229374292864	66.45571421241527	15.521152733202104	19.244942	118.904	-10.06363	11.395764	1.9788427	13.038091	4.7377243	8.969254	5.425513	1.3522661	0.54579365	0.32762027
3309541170817293824	68.66689038204488	15.208964911975178	21.075073	103.15689	-35.85557	11.549942	2.0912971	3.344131	1.0991819	6.668379	4.2592897	0.36493292	0.2443392	0.13831078
3309336867813205760	68.52256353868661	14.21747714186208	18.199448	85.34915	-16.904617	11.629388	1.8422108	1.4415438	0.34694323	2.4431305	1.6714453	0.3399052	0.08429948	0.049661882
47917816253918720	66.311133667576857	18.973455972926324	18.569708	97.28108	-28.887608	11.957183	2.0487833	2.0377967	0.5246777	8.945428	7.500937	0.11225916	0.302151984	0.16694689
33195804646282304	66.3069538557209	17.268076545714347	19.312836	107.2612	-27.188425	11.992548	2.6850185	9.33254	2.704552	2.6169952	19.287603	2.0163822	1.5024871	0.81455195
33081522008457011072	71.33110100353422	13.574216271157622	19.19447	87.72377	-9.913272	12.024581	2.3941412	15.202123	4.3817663	9.862589	7.839013	0.86788297	0.77107835	0.41712388
3311162843092490496	65.96041133865042	14.921402707495972	25.659887	115.94731	-28.725637	12.134732	2.6072578	11.986289	3.320653	5.654087	4.5110784	0.85494554	0.39180115	0.18730214
3307489031146701696	68.36303444839065	13.045385968619557	23.33511	110.45561	-21.440964	12.256755	2.342475	1.363789	0.2545818	2.3844779	2.0315888	0.16005203	0.08510464	0.041261565
3308428877366857728	70.366355522147463	14.076016738839469	26.182947	99.25034	-33.95699	12.363147	2.4602451	25.720503	7.026489	10.856859	10.731864	0.745237	1.2423422	0.56752026
3410409886514680064	69.01782417867581	18.888423253705223	20.245579	84.23755	-22.036737	12.4484824	2.47365	6.511168	1.7505827	11.434649	12.022853	0.21433577	0.76413935	0.3734725
47729215646206080	64.46150286122511	18.475053544960033	21.640215	113.170876	-30.777138	12.703422	2.698405	2.711683	0.7202027	2.0415013	2.0097606	0.49351305	0.12772296	0.059066143

Table 5 – continued

sourceid	RA	Dec	parallax	pmra	pmdec	mg	bppp	RUWEast	sigmabst	RUWESpec	sigmaspec	P	q	M_c
48455894049191424	63.624805023608	18.729881346946026	20.680376	110.10128	-30.568058	13.204377	2.7620544	3.769246	0.98915327	4.831599	7.9032397	0.18036395	0.43028054	0.18605632
49157794785448192	65.67911798706223	20.56998136359179	22.204473	109.14224	-37.47773	13.435896	2.8771925	10.13076	2.8767006	4.160689	7.6917205	0.50197315	0.66635245	0.2701574
3312613000147191680	67.9368293586253	15.630149907181586	21.92811	104.99937	-31.718637	13.436778	2.7022161	1.2680652	0.22256374	2.1944704	4.0981297	0.073810354	0.14576809	0.059358526
331103866698173184	65.84974595899124	14.4278449817287893	21.160046	110.94352	-21.135527	13.543492	2.9259453	12.498561	3.6824527	20.370281	41.5711	0.12476101	5.761253	2.334608
3313207698500079360	69.63189917287164	17.04055098240666	22.853317	106.24673	-31.3891	13.618415	2.808816	1.2659032	0.23495989	4.2582116	9.578849	0.031987548	0.282138	0.109801285
3314140599755959424	67.60020695729807	17.499587834144798	18.23571	78.77907	-28.804348	13.654834	2.7426186	10.872717	3.146904	2.9538498	6.8027906	0.79631144	0.6842594	0.28725055
3313839574086963712	65.39849909000245	16.894192274532255	24.33773	125.71914	-40.65925	13.948855	3.064352	8.383781	2.817	5.9499407	14.526592	0.23746127	1.244193	0.44788775
3310478710637066752	64.53629289150157	13.331259196596612	20.93439	111.15798	-14.546099	13.949699	2.8872652	1.5854778	0.4164988	4.107172	10.453021	0.056723293	0.3978708	0.15124361
3314137846679343872	68.0336649745617	17.6643440638911	21.075275	99.88685	-30.655151	13.979582	2.8372974	1.5255272	0.3941187	2.4364855	6.2334156	0.08940822	0.25801963	0.097356565
47760521664503296	65.11560537190881	18.89705576636259	19.672964	104.719475	-32.569706	13.988257	2.7881794	1.2785263	0.27335688	2.2563696	5.902441	0.070158176	0.21893603	0.08457476
3311221258944195200	65.66660974089085	15.062399584369444	23.376665	84.40576	-23.434784	14.077939	3.0911245	1.3902847	0.34179467	3.8369422	9.311588	0.046796	0.32785812	0.11720649
48509186003340416	62.776059616737115	18.928963628615932	19.93843	109.657745	-28.472279	14.192208	2.9350224	1.7115903	0.5110402	3.5404887	11.017797	0.069329664	0.46646634	0.17331943
48048902948906368	66.90245867179468	19.445767441293732	19.231146	96.80087	-38.773808	14.238761	3.0310307	16.237202	6.0698442	3.4705567	9.437445	0.99670756	1.3147694	0.4911199
3311102820926310784	65.39669553192954	14.695153868168017	20.326693	106.496574	-19.731718	14.278773	2.862668	1.3977338	0.3713231	2.7254941	9.875319	0.05512948	0.37344685	0.1358137
3311810047420637568	63.46857579356195	15.36487063340007	22.387419	123.95292	-13.587856	14.308949	2.9282503	1.5574532	0.4591437	5.319673	20.914965	0.029223839	0.7675065	0.26816785
3311804515502788352	63.273952149488956	15.247700118856342	22.357246	122.44951	-18.603453	14.355454	2.9613495	1.3029861	0.32675368	2.5205526	10.018484	0.04347603	0.35185495	0.12204755
47322297561027712	64.65025269592638	17.51585330705525	27.013884	64.83592	-61.09387	14.369595	2.959774	1.2812126	0.31491673	2.0114625	7.8232236	0.04440918	0.27206907	0.08790898
45198178534988672	62.490399744488908	15.416883616520483	21.22679	118.5227	-21.854282	14.58098	3.1423988	1.5162789	0.48248684	4.441856	20.385468	0.03322999	0.7961063	0.27099073
3410559832411244160	69.96546164739077	19.6593898461387	23.499067	87.291985	-34.13228	14.677451	3.234291	16.270372	7.1377497	3.6114807	11.025825	0.8210118	1.6573471	0.5350476
47959705067457152	66.12800628155945	18.986786982710726	20.498665	111.01914	-43.00263	14.982163	3.2060423	10.618676	5.2158256	2.239869	10.304867	0.7358764	1.39335447	0.44927633

stars. This gives us a rough estimate of the microlensing rate of $R \simeq 2\theta_E N_{\text{BH}} \Sigma_S v_{\text{H}} \simeq 2 \times 10^{-5} \text{ yr}^{-1}$, where we used $N_{\text{BH}} = 2$. Even if we consider astrometric lensing, for which the cross section for a measurable effect is larger (for example Miralda-Escude 1996; Paczynski 1996), the expected rate is too low. This is mainly because of the low number of background sources because of Hyades' location in the direction of the Galactic anticentre. Perhaps the orders of magnitude higher number of stars that will be found by LSST can improve this. More promising in the short term is to search for BHs in other OCs which are projected towards the Galactic centre.

5 CONCLUSIONS

In this study, we present a first attempt to find dynamical imprints of stellar-mass black holes (BHs) in Milky Way open clusters. In particular, we focused on the closest open cluster to the Sun, the Hyades cluster. We compared the mass density profiles from a suite of direct N -body models, conceived with the precise intent to model the present-day state of Hyades-like clusters (Wang & Jerabkova 2021), to radial mass distributions of stars with different masses, derived from *Gaia* data (Evans & Oh 2022).

Our comparison favours N -body models with 2–3 BHs at present. In these models, the presence of a central BH component quenches the segregation of visible stars, and leads to less concentrated distributions. Star clusters with 2–3 BHs (and a BH mass fraction $f_{\text{BH}} \simeq 0.1$) best reproduce the observed half-mass radius, while those that never possessed BHs display a value that is ~ 30 per cent smaller. This result is further confirmed by the radial distribution of high-mass stars ($m \geq 0.56 M_{\odot}$), which, being more segregated, are more affected by the presence of central BHs. Models in which the last BH was ejected recently (≤ 150 Myr ago) can still reproduce the density profile. For these models, we estimate that the ejected (binary) BHs are at a typical distance of ~ 60 pc from the Hyades.

Models with 2–3 BHs have a 1D dispersion in the innermost parsec of $\sim 350 \text{ m s}^{-1}$ compared to $\sim 250 \text{ m s}^{-1}$ for the no BH case and both are consistent with the available data. The tidal tails of models with and without BHs are almost indistinguishable.

In absence of primordial binaries, about 94 per cent of the BHs in the present-day state of our N -body models dynamically couple with other objects and form binary and triple systems. Among them, 50 per cent of the clusters with BHs host BH-star binary systems. Their period distribution peaks at $\sim 10^3$ yr making it unlikely to find BHs through velocity variations. We explored the possible candidate stars with a BH companion, based on their excess error in the *Gaia* single-source catalogue but otherwise high membership probability. We found 56 possible binaries candidates, but none which show strong evidence of sufficient companion mass to be a likely BH. Also, we explored the possibility to detect binary BHs through gravitational waves with Pulsar Timing Array. We found that (continuous) gravitational waves from a BBH in or near the Hyades is unlikely to be found. Finally, we estimated that detecting dormant BHs with gravitational microlensing is unlikely too.

Our study suggests that, at the present day, the radial mass distribution of stars provides the most promising discriminator to find signatures of BHs in open clusters. In particular, the most massive stars within the cluster, and their degree of mass segregation, represent the best tracers for the presence of central BHs. For the case of the Hyades, its present-day structure requires a significant fraction of BHs to form with kicks that are low enough to be retained by the host cluster.

Our approach of detailed modelling of individual OCs can be applied to other OCs to see whether Hyades is an unique cluster, or

that BHs in OCs are common. Charting the demographics in OCs in future studies will be a powerful way to put stringent constraints on BH kicks and the contribution of OCs to gravitational wave detections.

ACKNOWLEDGEMENTS

We thank the anonymous referee for the useful comments, which helped us to improve the quality of the manuscript. ST acknowledges financial support from the European Research Council for the ERC Consolidator grant DEMOBLACK, under contract no. 770017. MG acknowledges support from the Ministry of Science and Innovation (EUR2020-112157, PID2021-125485NB-C22, CEX2019-000918-M funded by MCIN/AEI/10.13039/501100011033) and from AGAUR (SGR-2021-01069). ZP acknowledges that this project has received funding from the European Research Council (ERC) under the European Union's Horizon 2020 research and innovation programme (Grant agreement No. 101002511 - VEGA P). LW thanks the support from the one-hundred-talent project of Sun Yat-sen University, the Fundamental Research Funds for the Central Universities, Sun Yat-sen University (22hytd09), and the National Natural Science Foundation of China through grant 12073090 and 12233013. FA acknowledges financial support from MCIN/AEI/10.13039/501100011033 through grants IJC2019-04862-I and RYC2021-031638-I (the latter co-funded by European Union NextGenerationEU/PRTR). ST thanks Michela Mapelli for valuable comments and suggestions.

DATA AVAILABILITY

The data underlying this article will be shared on reasonable request to the corresponding authors.

REFERENCES

- Aarseth S. J., 2003, *Gravitational N-Body Simulations*. Cambridge Univ. Press, Cambridge
- Alessandrini E., Lanzoni B., Ferraro F. R., Mocchi P., Vesperini E., 2016, *ApJ*, 833, 252
- Almeida A. et al., 2023, preprint (arXiv:2301.07688)
- Andrew S., Penoyre Z., Belokurov V., Evans N. W., Oh S., 2022, *MNRAS*, 516, 3661
- Antonini F., Gieles M., 2020a, *Phys. Rev. D*, 102, 123016
- Antonini F., Gieles M., 2020b, *MNRAS*, 492, 2936
- Antonini F., Rasio F. A., 2016, *ApJ*, 831, 187
- Askar A., Arca Sedda M., Giersz M., 2018, *MNRAS*, 478, 1844
- Bahcall J. N., Wolf R. A., 1976, *ApJ*, 209, 214
- Banerjee S., 2021, *MNRAS*, 500, 3002
- Banerjee S., Belczynski K., Fryer C. L., Berczik P., Hurley J. R., Spurzem R., Wang L., 2020, *A&A*, 639, A41
- Baumgardt H. et al., 2019, *MNRAS*, 488, 5340
- Baumgardt H., 2001, *MNRAS*, 325, 1323
- Belczynski K. et al., 2016b, *A&A*, 594, A97
- Belczynski K., Holz D. E., Bulik T., O'Shaughnessy R., 2016a, *Nature*, 534, 512
- Belokurov V. et al., 2020, *MNRAS*, 496, 1922
- Boekholt T., Portegies Zwart S., 2015, *Comput. Astrophys. Cosmol.*, 2, 2
- Bovy J., 2015, *ApJS*, 216, 29
- Brandner W., Calissendorff P., Kopytova T., 2023, *AJ*, 165, 108
- Cantat-Gaudin T. et al., 2018a, *A&A*, 615, A49
- Cantat-Gaudin T. et al., 2018b, *A&A*, 618, A93
- Cantat-Gaudin T., 2022, *Universe*, 8, 111
- Cantat-Gaudin T., Anders F., 2020, *A&A*, 633, A99
- Casamiquela L. et al., 2022, *A&A*, 664, A31

- Casertano S., Hut P., 1985, *ApJ*, 298, 80
- Castro-Ginard A. et al., 2020, *A&A*, 635, A45
- Castro-Ginard A. et al., 2022, *A&A*, 661, A118
- Castro-Ginard A., Jordi C., Luri X., Julbe F., Morvan M., Balaguer-Núñez L., Cantat-Gaudin T., 2018, *A&A*, 618, A59
- Chen X., Amaro-Seoane P., 2017, *ApJ*, 842, L2
- Chi H., Wang F., Wang W., Deng H., Li Z., 2023, *ApJS*, 266, 36
- Chomiuk L., Strader J., Maccarone T. J., Miller-Jones J. C. A., Heinke C., Noyola E., Seth A. C., Ransom S., 2013, *ApJ*, 777, 69
- Claydon I., Gieles M., Varri A. L., Heggie D. C., Zocchi A., 2019, *MNRAS*, 487, 147
- Claydon I., Gieles M., Zocchi A., 2017, *MNRAS*, 466, 3937
- Cropper M. et al., 2018, *A&A*, 616, A5
- Dalton G. et al., 2012, in McLean I. S., Ramsay S. K., Takami H., eds, Proc. SPIE Conf. Series Vol. 8446, Ground-based and Airborne Instrumentation for Astronomy IV. SPIE, Bellingham, p. 84460P
- de Jong R. S. et al., 2019, *The Messenger*, 175, 3
- de Vita R., Bertin G., Zocchi A., 2016, *A&A*, 590, A16
- Di Carlo U. N., Giacobbo N., Mapelli M., Pasquato M., Spera M., Wang L., Haardt F., 2019, *MNRAS*, 487, 2947
- Dickson N., Hénault-Brunet V., Baumgardt H., Gieles M., Smith P., 2023, *MNRAS* 522, 5320
- Djorgovski S., King I. R., 1986, *ApJ*, 305, L61
- Douglas S. T., Curtis J. L., Agüeros M. A., Cargile P. A., Brewer J. M., Meibom S., Jansen T., 2019, *ApJ*, 879, 100
- El-Badry K., Burdge K. B., 2022, *MNRAS*, 511, 24
- Evans N. W., Oh S., 2022, *MNRAS*, 512, 3846
- Fleck J. J., Boily C. M., Lançon A., Deiters S., 2006, *MNRAS*, 369, 1392
- Fryer C. L., Belczynski K., Wiktorowicz G., Dominik M., Kalogera V., Holz D. E., 2012, *ApJ*, 749, 91
- Fukushige T., Heggie D. C., 2000, *MNRAS*, 318, 753
- Gaia Collaboration 2016, *A&A*, 595, A1
- Gaia Collaboration 2018a, *A&A*, 616, A1
- Gaia Collaboration 2018b, *A&A*, 616, A10
- Gaia Collaboration et al.2023, *A&A*, 674, A1
- Geller A. M., Latham D. W., Mathieu R. D., 2015, *AJ*, 150, 97
- Gieles M., Erkal D., Antonini F., Balbinot E., Peñarrubia J., 2021, *Nat. Astron.*, 5, 957
- Giersz M., Heggie D. C., 2011, *MNRAS*, 410, 2698
- Giesers B. et al., 2018, *MNRAS*, 475, L15
- Giesers B. et al., 2019, *A&A*, 632, A3
- Goodman J., 1984, *ApJ*, 280, 298
- Goodman J., Heggie D. C., Hut P., 1993, *ApJ*, 415, 715
- Heggie D. C., 1975, *MNRAS*, 173, 729
- Hénault-Brunet V., Gieles M., Sollima A., Watkins L. L., Zocchi A., Claydon I., Pancino E., Baumgardt H., 2019, *MNRAS*, 483, 1400
- Hénon M., 1965, *Ann. Astrophys.*, 28, 992
- Hills J. G., Fullerton L. W., 1980, *AJ*, 85, 1281
- Hobbs G., Lorimer D. R., Lyne A. G., Kramer M., 2005, *MNRAS*, 360, 974
- Hunt E. L., Reffert S., 2021, *A&A*, 646, A104
- Hunt E. L., Reffert S., 2023, *A&A*, 673, A114
- Hurley J. R., 2007, *MNRAS*, 379, 93
- Hurley J. R., Pols O. R., Tout C. A., 2000, *MNRAS*, 315, 543
- Hurley J. R., Tout C. A., Pols O. R., 2002, *MNRAS*, 329, 897
- Janet F. A., Creighton T., Lommen A., 2005, *ApJ*, 627, L125
- Jerabkova T., Boffin H. M. J., Beccari G., de Marchi G., de Bruijne J. H. J., Prusti T., 2021, *A&A*, 647, A137
- Kopytova T. G., Brandner W., Tognelli E., Prada Moroni P. G., Da Rio N., Röser S., Schilbach E., 2016, *A&A*, 585, A7
- Kremer K. et al., 2020, *ApJS*, 247, 48
- Kroupa P., 2001, *MNRAS*, 322, 231
- Kulkarni S. R., Hut P., McMillan S., 1993, *Nature*, 364, 421
- Kumamoto J., Fujii M. S., Tanikawa A., 2020, *MNRAS*, 495, 4268
- Küpper A. H. W., Kroupa P., Baumgardt H., Heggie D. C., 2010, *MNRAS*, 401, 105
- Küpper A. H. W., Lane R. R., Heggie D. C., 2012, *MNRAS*, 420, 2700
- Küpper A. H. W., MacLeod A., Heggie D. C., 2008, *MNRAS*, 387, 1248
- Lindgren L. et al., 2021, *A&A*, 649, A2
- Liu L., Pang X., 2019, *ApJS*, 245, 32
- Lodieu N., Smart R. L., Pérez-Garrido A., Silvotti R., 2019, *A&A*, 623, A35
- Maccarone T. J., Kundu A., Zepf S. E., Rhode K. L., 2007, *Nature*, 445, 183
- Mackey A. D., Wilkinson M. I., Davies M. B., Gilmore G. F., 2007, *MNRAS*, 379, L40
- Mackey A. D., Wilkinson M. I., Davies M. B., Gilmore G. F., 2008, *MNRAS*, 386, 65
- Madsen S., 2003, *A&A*, 401, 565
- Makarov V. V., Odenkirchen M., Urban S., 2000, *A&A*, 358, 923
- Mandel I., de Mink S. E., 2016, *MNRAS*, 458, 2634
- Mapelli M., Colpi M., Possenti A., Sigurdsson S., 2005, *MNRAS*, 364, 1315
- Meingast S., Alves J., 2019, *A&A*, 621, L3
- Meingast S., Alves J., Rottensteiner A., 2021, *A&A*, 645, A84
- Merritt D., 2001, *ApJ*, 556, 245
- Merritt D., Piatek S., Portegies Zwart S., Hemsendorf M., 2004, *ApJ*, 608, L25
- Miller-Jones J. C. A. et al., 2015, *MNRAS*, 453, 3918
- Miralda-Escude J., 1996, *ApJ*, 470, L113
- Miyamoto M., Nagai R., 1975, *PASJ*, 27, 533
- Moe M., Di Stefano R., 2017, *ApJS*, 230, 15
- Navarro J. F., Frenk C. S., White S. D. M., 1995, *MNRAS*, 275, 720
- Nilakshi, Sagar R., Pandey A. K., Mohan V., 2002, *A&A*, 383, 153
- Odenkirchen M. et al., 2003, *AJ*, 126, 2385
- Offner S. S. R., Moe M., Kratter K. M., Sadavoy S. I., Jensen E. L. N., Tobin J. J., 2022, preprint (arXiv:2203.10066)
- Oh S., Evans N. W., 2020, *MNRAS*, 498, 1920
- Paczynski B., 1996, *ARA&A*, 34, 419
- Pavlík V., Jeřábková T., Kroupa P., Baumgardt H., 2018, *A&A*, 617, A69
- Penoyre Z., Belokurov V., Evans N. W., 2022, *MNRAS*, 513, 2437
- Penoyre Z., Belokurov V., Wyn Evans N., Everall A., Kopusov S. E., 2020, *MNRAS*, 495, 321
- Perryman M. A. C. et al., 1998, *A&A*, 331, 81
- Peuten M., Zocchi A., Gieles M., Gualandris A., Hénault-Brunet V., 2016, *MNRAS*, 462, 2333
- Piatti A. E., 2020, *A&A*, 639, A55
- Pittordis C., Sutherland W., 2019, *MNRAS*, 488, 4740
- Plummer H. C., 1911, *MNRAS*, 71, 460
- Portegies Zwart S. F., McMillan S. L. W., 2000, *ApJ*, 528, L17
- Rastello S., Amaro-Seoane P., Arca-Sedda M., Capuzzo-Dolcetta R., Fragione G., Tosta e Melo L., 2019, *MNRAS*, 483, 1233
- Rastello S., Carraro G., Capuzzo-Dolcetta R., 2020, *ApJ*, 896, 152
- Reino S., de Bruijne J., Zari E., d'Antona F., Ventura P., 2018, *MNRAS*, 477, 3197
- Rodríguez C. L., Chatterjee S., Rasio F. A., 2016, *Phys. Rev. D*, 93, 084029
- Röser S., Schilbach E., 2019, *A&A*, 627, A4
- Röser S., Schilbach E., Goldman B., 2019, *A&A*, 621, L2
- Röser S., Schilbach E., Piskunov A. E., Kharchenko N. V., Scholz R. D., 2011, *A&A*, 531, A92
- Samsing J. et al., 2022, *Nature*, 603, 237
- Sana H. et al., 2012, *Science*, 337, 444
- Saracino S. et al., 2022, *MNRAS*, 511, 2914
- Saracino S. et al., 2023, *MNRAS*, 521, 3162
- Sigurdsson S., Phinney E. S., 1993, *ApJ*, 415, 631
- Sim G., Lee S. H., Ann H. B., Kim S., 2019, *J. Kor. Astron. Soc.*, 52, 145
- Spitzer L., 1987, *Dynamical Evolution of Globular Clusters*. Princeton Univ. Press, Princeton
- Strader J., Chomiuk L., Maccarone T. J., Miller-Jones J. C. A., Seth A. C., 2012, *Nature*, 490, 71
- Tarricq Y., Soubiran C., Casamiquela L., Castro-Ginard A., Olivares J., Miret-Roig N., Galli P. A. B., 2022, *A&A*, 659, A59
- The LIGO Scientific Collaboration et al.2021, preprint (arXiv:2111.03606)
- Tornamenti S., Bertin G., Bianchini P., 2019, *A&A*, 632, A67
- Tornamenti S., Rastello S., Mapelli M., Di Carlo U. N., Ballone A., Pasquato M., 2022, *MNRAS*, 517, 2953
- van Straten W., Bailes M., Britton M., Kulkarni S. R., Anderson S. B., Manchester R. N., Sarkissian J., 2001, *Nature*, 412, 158

- Vesperini E., Hong J., Webb J. J., D'Antona F., D'Ercole A., 2018, *MNRAS*, 476, 2731
- Vesperini E., McMillan S. L. W., D'Antona F., D'Ercole A., 2013, *MNRAS*, 429, 1913
- Wang L., Hernandez D. M., 2021, preprint ([arXiv:2104.10843](https://arxiv.org/abs/2104.10843))
- Wang L., Iwasawa M., Nitadori K., Makino J., 2020b, *MNRAS*, 497, 536
- Wang L., Jerabkova T., 2021, *A&A*, 655, A71
- Wang L., Nitadori K., Makino J., 2020a, *MNRAS*, 493, 3398
- Wang L., Tanikawa A., Fujii M. S., 2022, *MNRAS*, 509, 4713
- Weatherford N. C., Chatterjee S., Kremer K., Rasio F. A., 2020, *ApJ*, 898, 162
- Wen L., 2003, *ApJ*, 598, 419
- Zhang Y., Tang S.-Y., Chen W. P., Pang X., Liu J. Z., 2020, *ApJ*, 889, 99
- Zocchi A., Gieles M., Hénault-Brunet V., 2019, *MNRAS*, 482, 4713

This paper has been typeset from a $\text{\TeX}/\text{\LaTeX}$ file prepared by the author.